

A functional tool to explore the reliability of micro-earthquake focal mechanism solution for seismotectonic purposes

G.M. Adinolfi ^{1,3,*}, R. De Matteis ¹, R. de Nardis ^{2,3} and A. Zollo ⁴

¹ Dipartimento di Scienze e Tecnologie, Università del Sannio ViaDe Sanctis, 82100 Benevento, Italy

² Dipartimento di Scienze Psicologiche, della Salute e del Territorio, Università di Chieti-Pescara “G. d’Annunzio”, Via dei Vestini, 32, 66100, Chieti, Italy

³ CRUST Centro interUniversitario per l’analisi SismoTettonica tridimensionale, Italy

⁴ Dipartimento di Fisica, Università di Napoli “Federico II”, Complesso Universitario di Monte S. Angelo, via Cinthia, 80124 Napoli, Italy

* Corresponding author: gmadinolfi@unisannio.it

ABSTRACT

Improving the knowledge of seismogenic faults requires the integration of geological, seismological, and geophysical information. Among several analyses, the definition of earthquake focal mechanisms plays an essential role in providing information about the geometry of individual faults and the stress regime acting in a region. Fault plane solutions can be retrieved by several techniques operating in specific magnitude ranges, both in the time and frequency domain and using different data. For earthquakes of low magnitude, the limited number of available data and their uncertainties can compromise the stability of fault plane solutions. In this work, we propose a useful methodology to evaluate how well a seismic network, used to monitor natural and/or induced micro-seismicity, estimates focal mechanisms as a function of magnitude, location, and kinematics of seismic source and consequently their reliability in defining seismotectonic models. To study the consistency of focal mechanism solutions, we use a Bayesian approach that jointly inverts the P/S long-period spectral-level ratios and the P polarities to infer the fault-plane solutions. We applied this methodology, by computing synthetic data, to the local seismic network operating in the Campania-Lucania Apennines (Southern Italy) aimed to monitor the complex normal fault system activated during the Ms 6.9, 1980 earthquake. We demonstrate that the method we propose is effective and can be adapted for other case studies with a double purpose. It can be a valid tool to design or to test the performance of local seismic networks and more generally it can be used to assign an absolute uncertainty to focal mechanism solutions fundamental for seismotectonic studies.

40 INTRODUCTION

41

42 Fault plane solutions represent primary information ~~that seismologists can retrieve~~ to describe the
43 earthquake source. The assessment of earthquake location, magnitude, and focal mechanism are the
44 fundamental operations to characterize the earthquake source through the point-source approximation.
45 ~~After the earthquake location, origin time, and source dimension are identified,~~ the focal mechanism
46 describes the basic geometry and kinematics of a point source in terms of strike, dip, and rake of the
47 fault plane along which the earthquake occurred. So, the focal mechanism is the most important
48 ~~parameter that can be retrieved to recognize~~ the geometry of the seismogenic faults and their style of
49 faulting. Moreover, ~~the seismicity and focal mechanisms of events, also of small magnitudes,~~ are often
50 used to constrain seismotectonic models, individual seismogenic sources, the regional strain, and stress
51 fields. Consequently, an evaluation of their effective reliability becomes a fundamental issue in
52 seismotectonic studies.

53 Nevertheless, focal mechanisms cannot be calculated and constrained every time an earthquake occurs.
54 Although the calculation of focal mechanisms represents a routine analysis ~~inside the~~ seismological
55 agencies, the solutions are calculated only for a specific range of magnitude, usually greater than 4. In
56 fact, constraining the solution for earthquakes with small magnitude ~~still represents~~ a challenge, despite
57 the advancement in the technological process and the use of increasingly performing seismic networks.
58 This is due to several factors that we will analyse in detail. The techniques used to define the focal
59 mechanism of large-moderate earthquakes are based on the inversion of the moment tensor, ~~that~~
60 corresponds to a stable and robust procedure, so much that it is the most common method for this
61 type of analysis (Dreger, 2003; Delouis, 2014; Sokos and Zahradnik, 2013; Cesca et al., 2011). This
62 technique requires accurate knowledge of the propagation medium in relation to the range of
63 frequencies used for the modelling ~~of the~~ waveforms recorded during an earthquake. The smaller an
64 earthquake, the higher the frequency range of the signal to be modelled, the more detailed the
65 knowledge and scale of the Earth's interior must be. Several methods have been proposed to achieve
66 a stable inversion of the moment tensor for earthquakes with a magnitude less than 3. Hybrid approach

67 ~~of the~~ amplitude and waveform moment tensor ~~inversions, which utilizes~~ the principal component
68 analysis of seismograms (Vavrycuk et al., 2017) or moment tensor refinement techniques (Kwiatek et
69 al. 2016; Bentz et al., 2018) facilitate a robust determination of the source type and its kinematics. In
70 particular, the retrieved moment tensor is typically decomposed into volumetric and deviatoric
71 components. Constraining the earthquake as ~~a~~ double-couple source can erroneously affect the retrieved
72 fault plane solutions, especially in the case of induced seismicity where the volumetric or non-double
73 couple component must be considered (Kwiatek et al. 2016).

74 Other analytical techniques are based on the recognition of radiation pattern ~~that describes the~~
75 ~~earthquake source~~. According to the position of seismic stations ~~with respect~~ to the source, seismic
76 waves on seismograms show different amplitudes and polarities. These features ~~are employed in a very~~
77 ~~simple way by several algorithms to~~ constrain the geometry of the earthquake faulting through
78 estimating the angular parameters strike, dip, and rake. The classical method (Raesenberg and
79 Oppenheimer, 1985;) uses the P-wave polarities, ~~but advanced ones use P- or S- wave amplitudes or~~
80 ~~amplitude ratios together with first motions (Snook, 2003) to~~ better constrain the focal mechanism of
81 small earthquakes. In fact, the use of polarities alone is not convenient, especially if we consider micro-
82 seismicity ($M < 3$). The reasons could be the limited number of available data, their uncertainties, and
83 the difficulty of measuring the P-polarity with a sufficient degree of precision. For these reasons,
84 different techniques using different types of measurements such as P-wave amplitudes (Julian and
85 Foulger, 1996; Tarantino et al., 2019), P/S or S/P amplitude ratios measured in the time or the
86 frequency domain (Kisslinger et al., 1981; Rau et al., 1996; Hardebeck and Shearer, 2003; De Matteis
87 et al., 2016), or S-wave polarizations (Zollo and Bernard, 1991) have been developed. The joint
88 inversion of polarities and amplitude ratios led to more stable and robust solutions, allowing to account
89 for geological site effects and to decrease ~~in first approximation~~ the effects produced by the geometric
90 and anelastic attenuations.

91 Two kinds of errors generally influence the goodness of the solution and retrieved model (Michele et
92 al., 2016): the perturbation errors that are related to how the uncertainty on data affects the model,

93 and the resolution errors that are referred to the capability to retrieve a correct model, given a dataset
94 as input or how accurate could be the model that we can recover, even if error-free data are used. The
95 sum of perturbation and resolution errors corresponds to the final errors on the model obtained by
96 solving an inverse problem, as the solution of focal mechanism. In particular, the resolution errors
97 depend on the available data, and so on the initial condition of the inverse problem. In the case of focal
98 mechanism, the number of seismic stations, as well as the seismic network geometry, and the velocity
99 structure of the crust influence the resolution and the reliability of the retrieved model.

100 How will the geometry of a seismic network determine the accuracy of focal mechanism solutions? The
101 answer to this question is not simple and requires a deep knowledge of the geophysical and geological
102 characteristics of the region, often unrealistic. Moreover, the theoretical relationships that predict the
103 focal mechanism solutions for an earthquake scenario could be very complicated if several factors, such
104 as network configuration, noise level, source magnitude, or source kinematics are taken into account.
105 ~~We want to underline that a~~ network configuration may be optimal for earthquake locations, but not for
106 retrieving fault plane solutions (Hardt and Scherbaum, 1994). In fact, a given geometry may resolve
107 some fault kinematics better than others.

108 A seismic network layout is strictly associated with the goals of the network and the available funds;
109 according to these features, a network operator decides how many stations are required and where
110 they should be located (Havskov et al.; 2011). So, the number of seismic stations, the size, and geometry
111 of the network are defined after a preliminary phase based on the evaluation of the specific
112 seismological target (Trnkoczy et al., 2009; Hardt and Scherbaum 1994; Steinberg et al. 1995; Bartal
113 et al. 2000). In the case of small earthquakes, the available recordings come from only a portion of the
114 total network, while the distant stations show a seismic signal buried in the noise. In order to detect
115 and locate low-magnitude earthquakes, we must increase the number of seismic stations for area units
116 by building a dense seismic network.

117 In this study, we propose a useful tool to evaluate both 1) the reliability of focal mechanism solutions
118 inferred by the inversion of different seismological data and 2) the performance of the seismic network

119 to assess focal mechanism solutions and their errors. We evaluate the network capability to solve focal
120 mechanisms as a function of magnitude, location, and kinematics of seismic source. We consider three
121 synthetic data set: P-wave polarities, P- S-wave amplitude spectral ratios and polarities and amplitude
122 ratios together. Moreover, different levels of noise are considered in order to simulate more realistic
123 conditions.

124 We selected as target the Irpinia Seismic Network (ISNet), a local seismic network that monitors the
125 Irpinia complex normal fault system (Southern Italy), activated during the Ms 6.9 earthquake of 23rd
126 November 1980. Evaluating the specific performance of an existing network for a seismological goal is
127 critical and can be used to decide how to improve its layout.

129 METHODOLOGY

130 With the main aim to define the reliability of focal mechanisms retrieved by specific seismic networks,
131 we propose a methodology based on an empirical approach that consists of different steps.

132 ***Configuration and Parameter Tuning (Step 1)***. In a preliminary phase, we select for each earthquake
133 simulation the: a) fault plane solution to test, b) seismic observables to be computed (i.e. P-wave
134 polarities or P- S-wave amplitude spectral ratios), c) magnitude, d) the earthquake epicentre and depth;
135 e) the network geometry; f) the noise level. The fault plane solution to test can be derived from
136 instrumental seismicity as one of the strongest earthquakes occurred in the area or a median solution
137 of the available ones or simply a fault plane solution representative of the regional seismotectonic.
138 Once the network geometry and the hypocentre of the earthquake are defined, the seismic stations
139 (number and type) for which the synthetic data are computed must be selected. The number of seismic
140 stations that record an event depends on earthquake magnitude, source-stations distance, crustal
141 medium properties, and the level of noise. We use an empirical approach, based on the statistical
142 analysis of the local seismicity catalog, that allows us to define, for each magnitude range, a maximum

143 (threshold) epicentral distance for which only the seismic stations within this distance are considered
144 (See data analysis).

145 ***Synthetic Data Computation (Step 2).*** Using a crustal velocity model and the source-receiver relative
146 position, the synthetic data are computed for the theoretical fault plane solution. The seismic
147 observables that can be reproduced are a) P-wave polarities, b) P/S spectral amplitude ratios, and c)
148 polarities and amplitude ratios together. For the P/S spectral level ratios, the Gaussian noise level is
149 added.

150 ***Focal Mechanism Inversion (Step 3).*** We estimated focal mechanism using BISTROP code (De Matteis
151 et al., 2016) that jointly inverts the ratio between the P- and S-wave long-period spectral levels and
152 the P-wave polarities according to a Bayesian approach. BISTROP has the advantage to use different
153 observables for the determination of fault plane solutions, such as the P/S long-period spectral level
154 ratios or P-wave polarities, individually or together. The benefits of the use of spectral level ratios are
155 multiples: 1) they can be measured for a broad range of magnitudes (also for $M < 3$; De Matteis et al.,
156 2016); 2) they can be calculated by automatic procedures without visual inspection; 3) their estimates
157 do not require to identify the first arrival time accurately, but only a time window of signal containing
158 P- or S-phase is mandatory and 4) the spectral amplitude ratios, they can generally be used without
159 the exact knowledge of the geological soil conditions (site effects) and geometric/anelastic attenuation.
160 Moreover, the joint inversion of amplitude spectral ratios and polarities led to constraining fault plane
161 solutions reducing the error associated with the estimates of retrieved parameters. BISTROP solves an
162 inverse problem through a probabilistic formulation leading to a complete representation of uncertainty
163 and correlation of the inferred parameters.

164 For a double-couple seismic source, the radiation pattern depends on fault kinematics and relative
165 source-station position. In fact, it can be represented as a function of 1) strike, dip and rake angles (φ ,
166 δ , λ) and 2) take-off and azimuth angles (i_h , φ_r). We can define the ratio between P- and S-wave
167 radiation pattern coefficients as:

$$\frac{\mathcal{R}^P(\phi, \delta, \lambda, i_h, \phi_R)}{\mathcal{R}^S(\phi, \delta, \lambda, i_h, \phi_R)} = \left(\frac{\alpha_s^2 \alpha_r}{\beta_s^2 \beta_r} \right) \frac{\Omega_0^P}{\Omega_0^S} \quad (1)$$

where Ω_0^P and Ω_0^S are the long-period spectral level of the P- and S-waves, respectively, and $\alpha_s, \alpha_r, \beta_s, \beta_r$, are the P- and S-wave velocities at the source and at the receiver, respectively. Thus, using the displacement spectra, assuming a given source and attenuation model (Boatwright, 1980), we can derive from the signal recorded by a seismic station the ratio of radiation pattern coefficients for P- and S-phases, as well as $\alpha, \beta, i_h, \phi_r$ are known from the earthquake location and the velocity model used. So, from a theoretical point of view, the spectral amplitude ratios measured at several seismic stations can be used to retrieve the ratio of radiation pattern coefficients $\mathcal{R}_{\theta\phi}^P/\mathcal{R}_{\theta\phi}^S$ as a function of the source-receiver azimuth and take-off angles.

BISTROP jointly inverts the spectral amplitude ratios with the observed P-wave polarities to infer the parameters ϕ, δ, λ of the focal mechanism in a Bayesian framework. A posterior probability density function (PDF), for the vector of model parameter \mathbf{m} (ϕ, δ, λ) and the vector of observed data \mathbf{d} , is defined as:

$$q(\mathbf{m}|\mathbf{d}) = \frac{f(\mathbf{d}|\mathbf{m})p(\mathbf{m})}{\int_M f(\mathbf{d}|\mathbf{m}')p(\mathbf{m}') d\mathbf{m}'} \quad (2)$$

where $f(\mathbf{d}|\mathbf{m})$ is the conditional probability function that represents the PDF given the data \mathbf{d} and for parameter vector \mathbf{m} in the model parameter space M , and $p(\mathbf{m})$ is the a priori PDF. If P-wave polarities and P/S spectral level ratios are independent datasets, the conditional probability function may be written as:

$$f(\mathbf{d}|\mathbf{m}) = f(\mathbf{d}^L|\mathbf{m})f(\mathbf{d}^P|\mathbf{m}). \quad (3)$$

190 in which the pdf of the data vector \mathbf{d}^L of N^L measurements of spectral ratios is multiplied for the pdf
 191 of data vector \mathbf{d}^P of N^P measurements of P-wave polarities given the model \mathbf{m} .

192 Assuming that the observables have the same finite variance, for the N^L observations of spectral level
 193 ratios the conditional probability function may be defined as:

$$194 \quad f(\mathbf{d}^L|\mathbf{m}) = \frac{1}{(\sqrt{2\pi}\sigma)^{N^L}} \exp\left(-\frac{\sum_{i=1}^{N^L}\{d_i - [G(\mathbf{m})]_i\}^2}{2\sigma^2}\right) \quad (4)$$

195

196 Where $G(\mathbf{m})$ represents a functional relationship between model and data and corresponds to Equation
 197 1 and σ represents the uncertainty on the spectral measure.

198 For the N^P observations of P-wave polarities, the conditional probability function is (Brillinger et al.,
 199 1980):

$$200 \quad f(\mathbf{d}^P|\mathbf{m}) = \prod_{i=1}^{N^P} \frac{1}{2} [1 + \psi(\mathcal{R}_i^P, \gamma_i, \rho_0) Y_i \text{sign}(\mathcal{R}_i^P)] \quad (5)$$

201

202 in which:

203 .

$$204 \quad \psi(\mathcal{R}_i^P, \gamma_i, \rho_0) = (1 - 2\gamma_i) \text{erf}(|\rho_0 \mathcal{R}_i^P(\mathbf{m})|) \quad (6)$$

205

206 The quantity reported in square brackets in Equation 5 represents the probability that the observed i_{th}
 207 polarity γ_i is consistent with the theoretical one computed from the model \mathbf{m} , whose theoretical P-wave
 208 amplitude is \mathcal{R}_i^P and $\text{sign}(\mathcal{R}_i^P)$ is its polarity at i_{th} station for a given fault plane solution. The
 209 parameters ρ_s and γ_0 , referring to the errors in ray tracing due to velocity model ambiguity and to the

210 uncertainty on polarity reading, regulating the shape of the PDF. For more details about the
211 mathematical formulation, see De Matteis et al. (2016).

212 *Evaluation of the Results (Step 4).* Once the best solution is estimated, the focal mechanism
213 uncertainties and its misfit, respect to the theoretical solution as Kagan angle, are computed. The focal
214 mechanism parameter (strike, dip and rake) misfit and their uncertainties are also calculated.

215

216 IRPINIA SEISMIC NETWORK

217 As testing case of our methodology, we choose the area of the M 6.9, 1980 Irpinia earthquake
218 (Southern Italy). Since 2005, ISNet, a local, dense seismic network monitors the seismicity along the
219 Campania-Lucania Apennines covering an area of about $100 \times 70 \text{ km}^2$ (Figure 1; Weber et al., 2007).
220 The seismic stations are deployed within an elliptic area whose major axis, parallel to the Apennine
221 chain, has a NW-SE trend with an average inter-stations distance of 15 km that reaches 10 km in the
222 inner central zone. Each seismic station ensures a high dynamic range and it is equipped with a strong-
223 motion accelerometer, Guralp CMG-5T or Kinematics Episensor, and a short period three-component
224 seismometer, Geotech S13-J with a natural period of 1 sec. In 6 cases, broadband seismometers are
225 installed such as the Nanometrics Trillium with a flat response in the range 0.025–50 Hz. ISNet is
226 operating by INFO (Irpinia Near Fault Observatory) and it provides real-time data at local control centres
227 for earthquake early warning systems or real-time seismic monitoring (Satriano et al., 2011). Seismic
228 events are automatically identified and located from continuous recordings by automatic Earth-worm
229 Binder and data are then manually revised by operators (Festa et al., 2020).

230 The 1980, M 6.9, Irpinia earthquake was one of the most destructive, instrumental earthquakes of the
231 Southern Apennines, causing about 3000 fatalities and severe damages in the Campania and Basilicata
232 regions. It activated a NW-SE trending normal fault system with a complex rupture process involving
233 multiple fault segments according to (at least) three different nucleation episodes delayed each other
234 of 20 s (Bernard and Zollo, 1989; Pantosti and Valensise; 1993; Amoroso et al.; 2005). No large

235 earthquakes occurred in the Irpinia region since 1980. A Mw 4.9 earthquake took place in 1996
236 originating a seismic sequence inside the epicentral area of the 1980 earthquake (Figure 1; Cocco et
237 al., 1999). Recent instrumental seismicity occurs mainly in the first 15 km of the crust showing fault
238 plane solutions with normal and normal-strike slip kinematics, indicating a dominant SW-NE extensional
239 regime (Pasquale et al., 2009; De Matteis et al., 2012; Bello et al., 2021). Low-magnitude seismicity
240 ($M_L < 3.6$) is spread into a large volume related to the activity of major fault segments of the 1980
241 Irpinia earthquake (Figure 1; Adinolfi et al., 2019; Adinolfi et al., 2020). Seismic sequences or swarms
242 often occurred in the area, extremely clustered in time (from several hours to a few days) and space
243 and seem to be controlled by high pore fluid pressure of saturated Apulian carbonates bounded by
244 normal seismogenic faults (Stabile et al., 2012; Amoroso et al., 2014).

245

246 DATA ANALYSIS

247 We applied the method we proposed and evaluated the capability of the ISNet local network to resolve
248 fault plane solutions using different observables as input data: a) P-wave polarities, b) P/S spectral
249 amplitude ratios and c) polarities and amplitude ratios together. the analysis is carried out by evaluating
250 the effect of 1) earthquake magnitude, 2) epicentral location, 3) earthquake depth, 4) signal-to-noise
251 ratio, and 5) fault kinematics on retrieved focal solutions as previously described.

252 **Step 1.** In order to select focal mechanisms (FMs) to be used for our resolution study (Figure 2a), we
253 carried out statistical analysis to define the most frequent fault plane solutions of instrumental
254 seismicity. We classified, according to the plunge of P- and T-axes, the fault plane solutions reported
255 in De Matteis et al. (2012) choosing only the FMs occurring within the Irpinia area since 2005 to 2011.
256 As shown in Figure 2b, splitting the range of the data into equal-sized bins, we selected the focal
257 mechanism corresponding to the median value of the most populated class. We report it in Figure 2a
258 as FM2. This corresponds to a normal-strike-slip fault plane solution with strike, dip, and rake equal to
259 292° , 53° , and -133° , respectively. Then, we decided to test the focal mechanism solution of the 1980

260 Irpinia earthquake, a pure normal fault (strike, dip, rake: 317° , 59° , -85° ; Westaway and Jackson, 1987;
261 Fig. 2a) here and after FM1. This solution is very similar to the focal mechanism corresponding to: 1)
262 the regional stress field (see Supplementary Material); 2) the M_L 2.9, Laviano earthquake, one of the
263 most energetic earthquakes of the last years (Stabile et al.; 2012), and 3) those of the 2nd, 3rd, 4th most
264 populated bins. Finally, we selected the solution corresponding to the 5th bin reported as FM3 in Figure
265 2a. This focal mechanism is quite different from the others due to a predominant component along the
266 fault strike (strike, dip, rake: 274° , 71° , -128°)

267 **Step 2.** For each of the three selected fault plane kinematics, we calculated synthetic data (P-wave
268 polarities or P- and S-wave spectral amplitudes) at seismic stations varying the earthquake location and
269 by using a local velocity model (Matrullo et al., 2013). We discretize the study area with a square grid
270 ($100 \times 100 \text{ km}^2$), centred on the barycentre of ISNet, with 441 nodes and a sampling step of 5 km.
271 Each node corresponds to a possible earthquake epicentre (Figure 3).

272 For each grid node and according to the earthquake magnitude to be tested, we have to select the
273 ISNet stations for simulations. The number of seismic stations that record an event depends on
274 earthquake magnitude, source-stations distance, crustal medium properties, and the noise level.
275 Theoretical relationships that link the seismic source to the signal recorded at every single station are
276 quite complicated (Kwiatek et al., 2016; 2020) and are based on the accurate knowledge of crustal
277 volumes in which the seismic waves propagated, such as the three-dimensional wave velocity structure,
278 anelastic attenuation or/and site conditions of a single receiver. To overcome this limitation, we used
279 an empirical approach to define the number and the distance of the seismic stations that record a
280 seismic signal as a function of magnitude, once its epicentral location (grid node) and depth are fixed.
281 Using the bulletin data retrieved by INFO at ISNet during the last two years (January 2019-March 2021;
282 <http://isnet-bulletin.fisica.unina.it/cgi-bin/isnet-events/isnet.cgi>), we selected two earthquake catalog
283 datasets with depths equal to 5 (+- 2) km and 10 (+- 2) km, respectively, and local magnitude ranging
284 between 1.0 and 2.5. These choices are motivated by the characteristics of the Irpinia micro-seismicity
285 recorded by ISNet. Then, we divided each dataset into bins of 0.5 magnitudes and for each bin, we

286 retrieved the median number of P-wave polarity readings and the median epicentral distance of the
287 farthest station that recorded the earthquake (Table 1). The bulletin data are manually revised by
288 operators, and we selected only seismic records that provide P- and/or S- wave arrival times. The
289 median value of the distance of the farthest station is then used to select the seismic stations for which
290 synthetic data are calculated. Therefore, for each earthquake simulation of specific magnitude and
291 depth, only the seismic stations with a distance, from the grid node under examination (epicentre), equal
292 or lower than the maximum distance, reported in Table 1, are considered. We run simulations only for
293 earthquakes recorded at least by 6 seismic stations. The synthetic P-wave polarities are simulated only
294 at a number of stations corresponding to the median value previously defined. (Table 1). We pointed
295 out that the number of P-wave polarities empirically assigned is related to the available earthquake
296 catalogue data of the Irpinia region where the seismicity can occur in different portions of the area
297 covered by the network, not always with optimal azimuthal coverage.

298 Additionally, we simulated the uncertainty on the measure of spectral level ratios or the effect of seismic
299 noise adding a zero mean, Gaussian noise to the synthetic data with a standard deviation equal to two
300 different percentage levels, as 5% and 30%. With this configuration, we simulated:

- 301 • Three datasets of seismic observables: P-wave polarities (D1), P/S spectral level ratios (D2) and
302 polarities and P/S spectral level ratios together (D3)
- 303 • Two hypocentre depths: 5 km and 10 km
- 304 • Three magnitude bins: M_L 1.0 - 1.5 (M1), M_L 1.5 - 2.0 (M2) and M_L 2.0 - 2.5 (M3)
- 305 • Three focal mechanism solutions: FM1 (317°, 59°, -85°), FM2 (292°, 53°, -133°) and FM3
306 (274°, 71°, -128°)

307 Two level of Gaussian noise: 5% and 30%. When D2 is simulated, in order to solve the verse ambiguity
308 of the slip vector, a P-wave polarity is added to the earthquake data to be inverted for the focal
309 mechanism.

310 **Step 3.** For each earthquake simulation the focal mechanism was estimated by inverting the synthetic
311 data with BISTROP (De Matteis et al.; 2016).

312 **Step 4.** In order to analyse the results, we defined five kinds of map to study how the focal mechanism
313 (FM) resolution and error spatially change in the area where ISNet is installed (Table 2):

314

- 315 • Kagan angle misfit map (KAM)
- 316 • Map of the focal mechanism parameter misfit (FMM)
- 317 • Strike, Dip and Rake error map (FME)
- 318 • Kagan angle average map (KAA)
- 319 • Kagan angle standard deviation map (KAS)

320

321 The Kagan Angle (KA) measures the difference between the orientations of two seismic moment tensors
322 or two double couples. It is the smallest angle needed to rotate the principal axes of one moment tensor
323 to the corresponding principal axes of the other (Kagan et al.; 1991; Tape and Tape; 2012). The smaller
324 the KA between two focal mechanisms, more similar they are. In KAM map, for each node the value of
325 KA between the theoretical and retrieved solution is reported, while in FMM map, the absolute value of
326 the misfit between the strike, dip, and rake angles of the retrieved and theoretical solution is indicated.
327 FME is defined as the error map of strike, dip, and rake in which the uncertainties (standard deviations)
328 are calculated considering all the solutions with probability larger than the 90% (S90) of the maximum
329 probability, corresponding to the best solution retrieved. Additionally, these solutions are used to study
330 how constrained is the FM solution. The KA is calculated between each FM of S90 solutions and the
331 retrieved best solution. The mean and the standard deviation of the resulting KA distribution are plotted
332 in KAA and KAS maps, respectively. The smaller KA mean and std, the more constrained is the obtained
333 fault plane solution (Table 2).

334

335 DISCUSSION

336 We consider the FM1, i.e. the focal mechanism of the 1980 Irpinia earthquake located at 10 km depth,
337 first. Looking at Figures 4 and 5, we see the effect of using the three different datasets. Considering

338 D1, we can calculate the FM only for earthquakes with magnitude 2.0-2.5 for which at least 6 polarities
339 are available. As shown by KAM map in Figure 4a, the retrieved solutions are characterized by high KA
340 ($> 50^\circ$) with limited areas or single nodes with values in the range 40° - 50° . Therefore, D1 is not
341 sufficient to retrieve with acceptable accuracy the FMs for earthquakes with magnitude 2.0-2.5. The
342 same result is obtained for FM2 and FM3 (Figure 4b-c). Comparing the results of the simulations using
343 D2 and D3 (Figure 5), the accuracy of the retrieved solution is improved when P-wave polarities data
344 are added to spectral level ratios. The areas in KAM map with high value of KA ($KA \geq 18^\circ$; red or green
345 areas) disappear or are strongly reduced. Nevertheless, ~~we want to underline that,~~ even with D2 dataset,
346 ~~exception some small areas,~~ the FMs are well retrieved for all magnitudes with the KA misfit mostly
347 lesser than 10° . The spatial resolution of the network is strongly influenced by the earthquake
348 magnitude. In fact, for both M1 and M2, there are nodes (white areas where we assume the $KA = -1$ as
349 an indeterminate value) for which the FMs cannot be calculated because ~~a minimum number of stations~~
350 ~~(at least 6)~~ are not available (Table 1). At the same time, the areas better resolved correspond to the
351 region inside the network, ~~although with D2 and D3 acceptable solutions are calculated for M1 and~~
352 M2 earthquakes also outside the network, (Figure 5).

353 Looking at Figure 6, using the D3 dataset, ~~we observe that, among the FM parameters,~~ the dip angle
354 is the best resolved compared with strike and rake angles. ~~Considering~~ M2 and M3 focal mechanisms,
355 the misfit of dip is very low ($< 8^\circ$), followed, in ascending order, by rake and strike that show higher
356 values ($10^\circ < \text{misfit} < 22^\circ$). For M1 (Figure 6a-d-g), rake and strike misfits are larger than 50° , with
357 rake worse resolved than strike. The unresolved areas correspond to the regions outside the seismic
358 network.

359 The KAA and KAS maps (Figures 7 and 8) show how the network constrains the fault plane solution as
360 a function of the epicentral location. Moreover, Figures 7d-e-f and 8d-e-f indicate that the areas with
361 KA mean and ~~std~~ greater than 30° and 20° , respectively, are reduced when P-wave polarities and
362 spectral level ratios data are used. On ~~contrary,~~ only for M1 focal mechanisms, there is no improvement
363 because the number of P-wave polarities is the same for both D2 and D3 datasets (Table 1). The worst
364 constrained regions correspond to a belt surrounding the seismic network, with KA mean $< 30^\circ$ and

365 KA std $< 20^\circ$ for M2 and M3 solutions. For M1, areas with high uncertainty remain outside and inside
366 the network, specifically in the central and eastern sectors.

367 Looking at the uncertainties of FM parameters, obtained by using the D3 dataset, Figure 9 shows that
368 the dip is the better-constrained parameter with an error $< 10^\circ$, also for M1 solutions. The rake angle
369 shows an uncertainty ~~lesser~~ $< 20^\circ$ for M2 and M3, while it ~~overcomes~~ 50° for M1. The strike angle
370 ~~reveals~~ the highest uncertainty, with values greater than 50° in the eastern and southern sectors of the
371 map for ~~all~~ analysed magnitudes (M1, M2, and M3). Accuracy improves moving from M1 to M3
372 earthquakes.

~~373 As shown in Figure 10, the accuracy of fault plane solutions, in terms of KA misfit calculated by using~~
374 ~~the D3 dataset, is similar for FM1, FM2, and FM3, mostly with values lesser than 8° for all the~~
375 ~~magnitudes M1, M2, and M3. FM2 and FM3 show a slightly higher precision than FM1 in the area~~
376 ~~inside the seismic network (see FMM, FME, KAA, and KAS maps for FM2 and FM3 in Supplementary~~
377 ~~Material). In the regions outside the network, where the azimuthal gap increases, the FMs better~~
378 ~~constrained in descending order are: FM3, FM2, and FM1. This effect should be due to the geometric~~
379 ~~relationship between the spatial distribution of the seismic stations and the orientation of the principal~~
380 ~~axes (P, T, B) that characterize the FMs.~~

381 Considering the effect of hypocentre depth, the results achieved for earthquakes at 5 km depth, ~~by~~
382 ~~using the D3 dataset, are overall unchanged (Figure 11). We note that the fault plane solutions are~~
383 ~~slightly worse resolved due to a smaller number of P-wave polarities available for M2 and M3. The KA~~
384 ~~misfit ~~mainly~~ is ~~lesser~~ $< 10^\circ$, even though the number and the dimension of areas with misfits $> 20^\circ$~~
385 ~~are greater than those obtained considering earthquakes at 10 km depth. Moreover, the dip angle~~
386 ~~shows a misfit lower than strike and rake angles for M1, M2, and M3; the accuracy of the retrieved FMs~~
387 ~~parameters is mainly ~~lesser~~ $< 8^\circ$, as shown in Figure 11.~~

388 Previous analyses are carried out considering ~~by using~~ data affected by 5% Gaussian error. In the last
389 test, we simulated synthetic data adding a 30% Gaussian error. As illustrated in Figure 12, FM solutions
390 show an overall larger misfit, in particular, the KA inside the seismic network is less than 20° . The area
391 best resolved (KA $< 8^\circ$) is ~~considerably~~ reduced to a ~~small~~ central portion of the network. This result

392 indicates that the accuracy of the spectral level ratio estimates is crucial: noisy waveforms with a low
393 signal-to-noise ratio can critically affect the result of the focal mechanism inversion. So, seismic noise
394 as well as the number of available stations, variable due to the operational condition, strongly influence
395 the capability of the seismic network to retrieve fault plane solution. Using the results of our simulations,
396 we classified the focal mechanism provided by De Matteis et al. (2016) according to a quality code
397 based on the resolution of fault kinematics (Table 3). In fact, we assigned to focal mechanisms of Irpinia
398 instrumental seismicity a quality A, B and C for the solutions that fall into the bins relative to FM3,
399 FM2 and FM1 kinematics, respectively. The quality A, B and C correspond to the average value of KA
400 misfit ($FM3=2.4^\circ$, $FM2=3.1^\circ$, $FM1=4.5^\circ$) calculated for M1, M2 and M3 magnitudes using D3 dataset
401 and considering earthquakes at 10 km depth with 5% Gaussian errors.

402 As last analysis, we carried out a test in a more general framework, without a fixed network
403 configuration. We explored the reliability of focal mechanism estimation as a function of the uniformity
404 focal sphere coverage defined by the number of recording seismic stations and azimuthal gap. We
405 simulated 10400 earthquakes fixing the fault plane solution and varying: 1) the number of seismic
406 stations (6-30), 2) take-off angle and 3) azimuth of each single station. For each possible number of
407 seismic stations, we run about 400 simulations, and we randomly sampled the focal sphere varying the
408 azimuth and take-off of the stations and, so, changing the geometrical configuration of our virtual
409 network of each simulation. We computed the KA between the theoretical and retrieved focal mechanism
410 (best) solutions, using only P-polarities, for each simulation. We show the results in the Figures 13 and
411 S7, as 3-D histograms and 3-D scatter plot, respectively. In the Figures 13a, as expected, we note that,
412 as the number of stations increases, the KA and its range of variation decrease. If the number of stations
413 is less than nine, only few solutions have $KA < 40^\circ$. Figure 13b shows that the most value of KA less
414 than 30° are obtained for azimuthal gap less than about 80° . Moreover, these evidences are shown in
415 the Figure S7, where the relation among the KA, azimuthal gap and number of stations is clear by the
416 three-dimensional spatial point patterns as well by the projections of the data on the three coordinate
417 planes.

418

CONCLUSIONS

We studied the focal mechanism reliability retrieved by the inversion of data recorded by ISNet, a local dense seismic network that monitors the Irpinia Fault System in Southern Italy. Three different datasets of seismological observables are used as input data for focal mechanism determination: a) P-wave polarities, b) P/S long-period spectral amplitude ratios and c) joint polarities and amplitude ratios. Starting from empirical observations, we computed synthetic data for a regular grid of epicentre locations at two depths (5 and 10 km), for earthquake magnitude in the range 1.0-2.5 and for three focal mechanism solutions. Two different levels of Gaussian error (5% and 30%) are added to the data.

~~Main conclusions can be summarized as follows.~~

- The joint inversion of P-wave polarities and P/S spectral amplitude ratios allows retrieving accurate FM (KA misfit $< 8^\circ$) also for earthquakes with magnitude ranging between 1.0 and 2.5, at depth of 5 and 10 km. Due to the low-energy magnitude, the number of P-wave polarities is not adequate to constrain fault plane solutions.
- The spatial resolution analysis of ISNet shows that the most accurate FM solutions are obtained for earthquakes located inside the network with strike, dip and rake misfit $< 8^\circ$. Nevertheless, outside the network or at its borders, acceptable solutions can be calculated even if the azimuthal coverage is not adequate (especially for M2 and M3 events). This peculiarity is due to the geometrical relationship between the recording seismic stations and the orientation of principal axes (P, T, B).
- The geometry of the network allows to well resolve fault plane solutions varying between normal and normal-strike focal mechanism with mainly strike, dip and rake misfit lesser than 10° for magnitude range 1.5-2.5. The network resolves a slightly better normal-strike fault plane solution than a pure normal focal mechanism.
- Among the FM parameters, the dip angle shows the lowest uncertainty. Strike and rake angles reveal higher errors especially for M 1-1.5 earthquakes in the region outside the seismic network.

- Dataset affected by 30% Gaussian error provide a worsening in the accuracy of the retrieved FMs. Although the high error level, the area of well resolved fault plane solutions (KA misfit < 20°) persists in the central part of the network, especially for M2 and M3.

The methodology described in this work can be a valid tool to design or to test the performance of local seismic networks, aimed at monitoring natural or induced seismicity. Moreover, given a network configuration, it can be used to evaluate the reliability of FMs or to classify the retrieved fault plane solutions that represent a fundamental information in seismotectonic studies. Although it is a theoretical study, many earthquake scenarios with several magnitude, locations and noise conditions can be simulated to mimic the real seismicity.

REFERENCES

- Adinolfi, G. M., Cesca, S., Picozzi, M., Heimann, S., & Zollo, A. (2019). Detection of weak seismic sequences based on arrival time coherence and empiric network detectability: an application at a near fault observatory. *Geophysical Journal International*, *218*(3), 2054-2065.
- Adinolfi, G. M., Picozzi, M., Cesca, S., Heimann, S., & Zollo, A. (2020). An application of coherence-based method for earthquake detection and microseismic monitoring (Irpinia fault system, Southern Italy). *Journal of Seismology*, *24*, 979-989.
- Amoroso, O., Ascione, A., Mazzoli, S., Virieux, J., & Zollo, A. (2014). Seismic imaging of a fluid storage in the actively extending Apennine mountain belt, southern Italy. *Geophysical Research Letters*, *41*(11), 3802-3809.
- Amoroso, A., Crescentini, L., & Scarpa, R. (2005). Faulting geometry for the complex 1980 Campania-Lucania earthquake from levelling data. *Geophysical Journal International*, *162*(1), 156-168.
- Bartal, Y., Somer, Z., Leonard, G., Steinberg, D. M., & Horin, Y. B. (2000). Optimal seismic networks in Israel in the context of the Comprehensive Test Ban Treaty. *Bulletin of the seismological society of America*, *90*(1), 151-165.
- Bello, S., De Nardis, R., Scarpa, R., Brozzetti, F., Cirillo, D., Ferrarini, F., ... & Lavecchia, G. (2021). Fault Pattern and Seismotectonic Style of the Campania–Lucania 1980 Earthquake (M w 6.9, Southern Italy): New Multidisciplinary Constraints. *Front. Earth Sci*, *8*, 608063.
- Ben-Menahem, A., and S. J. Singh (1981). *Seismic Waves and Sources*, 1108 p, Springer-Verlag, New York.
- Bentz, Stephan, P. Martínez-Garzón, G. Kwiatak, M. Bohnhoff, and J. Renner (2018). Sensitivity of Full Moment Tensors to Data Preprocessing and Inversion Parameters: A Case Study from the Salton Sea Geothermal Field. *Bull. Seismol. Soc. Am.* *108*, 588–603, doi 10.1785/0120170203
- Bernard, P., & Zollo, A. (1989). The Irpinia (Italy) 1980 earthquake: detailed analysis of a complex normal faulting. *Journal of Geophysical Research: Solid Earth*, *94*(B2), 1631-1647.
- Boatwright, J. (1980). A spectral theory for circular seismic sources; simple estimates of source dimension, dynamic stress drop, and radiated seismic energy, *Bull. Seismol. Soc. Am.*, **70** (7), 1–27.
- Brillinger, D. R., A. Udías, and B. A. Bolt (1980). A probability model for regional focal mechanism solutions, *Bull. Seism. Soc. Am.* **70**, 149- 170.
- Cesca, S., Heimann, S., Stammer, K., & Dahm, T. (2010). Automated procedure for point and kinematic source inversion at regional distances. *Journal of Geophysical Research: Solid Earth*, *115*(B6).
- Cocco, M., Chiarabba, C., Di Bona, M., Selvaggi, G., Margheriti, L., Frepoli, A., ... & Campillo, M. (1999). The April 1996 Irpinia seismic sequence: evidence for fault interaction. *Journal of Seismology*, *3*(1), 105-117.
- Delouis, B. (2014). FMNEAR: Determination of focal mechanism and first estimate of rupture directivity using near-source records and a linear distribution of point sources. *Bulletin of the Seismological Society of America*, *104*(3), 1479-1500.

- 537 De Matteis, R., Matrullo, E., Rivera, L., Stabile, T. A., Pasquale, G., & Zollo, A. (2012). Fault delineation and
538 regional stress direction from the analysis of background microseismicity in the southern Apennines, Italy.
539 *Bulletin of the Seismological Society of America*, 102(4), 1899-1907.
540
- 541 De Matteis, R., Convertito, V., & Zollo, A. (2016). BISTROP: Bayesian inversion of spectral-level ratios and
542 P-wave polarities for focal mechanism determination. *Seismological Research Letters*, 87(4), 944-954.
543
- 544 Dreger, D. S., Lee, W. H. K., Kanamori, H., Jennings, P. C., & Kisslinger, C. (2003). Time-domain moment
545 tensor INverse codel (TDMT-INVC) release 1.1. *International Handbook of Earthquake and Engineering*
546 *Seismology*, WHK Lee, H. Kanamori, PC Jennings, and C. Kisslinger (Editors), Vol. B, 1627.
547
- 548 Festa, G., Adinolfi, G. M., Caruso, A., Colombelli, S., De Landro, G., Elia, L., ... & Zollo, A. (2021). Insights
549 into Mechanical Properties of the 1980 Irpinia Fault System from the Analysis of a Seismic Sequence.
550 *Geosciences*, 11(1), 28.
551
- 552 Hardebeck, J., and M. Shearer (2003). Using S/P Amplitude Ratios to Constrain the Focal Mechanisms of
553 Small Earthquakes, *Bull. Seism. Soc. Am.* **93**, 6, pp. 2434–2444, December 2003.
554
- 555 Hardt, M., & Scherbaum, F. (1994). The design of optimum networks for aftershock recordings. *Geophysical*
556 *Journal International*, 117(3), 716-726.
557
- 558 Havskov, J., Ottemöller, L., Trnkoczy, A., Bormann, P. (2012): Seismic Networks. - In: Bormann, P. (Ed.),
559 *New Manual of Seismological Observatory Practice 2 (NMSOP-2)*, Potsdam : Deutsches
560 GeoForschungsZentrum GFZ, 1-65.
561
- 562 Julian, B. R., and G. R. Foulger (1996). Earthquake mechanisms from linear-programming inversion of
563 seismic-wave amplitude ratios, *Bull. Seism. Soc. Am.* **86** (4), 972-980.
564
- 565 Kagan, Y. Y. (1991). 3-D rotation of double-couple earthquake sources. *Geophysical Journal International*,
566 106(3), 709-716.
- 567 Kisslinger, C., J. R. Bowman, and K. Koch (1981). Procedures for computing focal mechanisms from local
568 (SV/P) z data, *Bull. Seism. Soc. Am.* **71** (6), 1719-1729.
- 569 Kwiatek, G., P. Martínez-Garzón, and M. Bohnhoff (2016). HybridMT: A MATLAB
570 Software Package for Seismic Moment Tensor Inversion and Refinement. *Seismol. Res.*
571 *Lett.*
572
- 573 Kwiatek, G. and Y. Ben-Zion (2016). Theoretical limits on detection and analysis of small earthquakes.
574 *Journal of Geophysical Research-Solid Earth* 121, doi 10.1002/2016JB012908
575
- 576 Kwiatek, G. and Y. Ben-Zion (2020). Detection Limits and Near-Field Ground Motions of Fast and Slow
577 Earthquakes. *Journal of Geophysical Research: Solid Earth* 125, e2019JB018935, doi
578 10.1029/2019JB018935
579
- 580 Matrullo E., R. De Matteis, C. Satriano, O. Amoroso, and A. Zollo (2013). An improved 1D seismic velocity
581 model for seismological studies in the Campania-Lucania region (Southern Italy), *Geophys. J. Int.* **195**, Issue
582 1, pp.460-473, doi: 10.1093/gji/ggt224.
583
- 584 Michele, M., S. Custódio, and A. Emolo (2014). Moment tensor resolution: case study of the Irpinia Seismic
585 Network, Southern Italy, *Bull. Seismol. Soc. Am.* **104**, 1348-1357, doi: 10.1785/0120130177.
586

- 587 Pantosti, D., & Valensise, G. (1990). Faulting mechanism and complexity of the November 23, 1980,
588 Campania-Lucania earthquake, inferred from surface observations. *Journal of Geophysical Research: Solid*
589 *Earth*, 95(B10), 15319-15341.
- 590
- 591 Pasquale, G., De Matteis, R., Romeo, A., & Maresca, R. (2009). Earthquake focal mechanisms and stress
592 inversion in the Irpinia Region (southern Italy). *Journal of seismology*, 13(1), 107-124.
- 593
- 594 Reasenber, P., & Oppenheimer, D. USGS (1985). FPFIT, FPLOT, and FPPAGE: Fortran computer
595 programs for calculating and displaying earthquake fault-plane solutions. *US Geol. Surv. Open-File Rept.*
596 85, 739.
- 597
- 598 Satriano, C., Elia, L., Martino, C., Lancieri, M., Zollo, A., & Iannaccone, G. (2011). PRESTo, the earthquake
599 early warning system for southern Italy: Concepts, capabilities and future perspectives. *Soil Dynamics and*
600 *Earthquake Engineering*, 31(2), 137-153.
- 601
- 602 Snoke, J. A., Lee, W. H. K., Kanamori, H., Jennings, P. C., & Kisslinger, C. (2003). FOCMEC: Focal
603 mechanism determinations. *International handbook of earthquake and engineering seismology*, 85, 1629-
604 1630.
- 605
- 606 Stabile, T. A., Satriano, C., Orefice, A., Festa, G., & Zollo, A. (2012). Anatomy of a microearthquake sequence
607 on an active normal fault. *Scientific reports*, 2(1), 1-7.
- 608
- 609 Steinberg, D. M., Rabinowitz, N., Shimshoni, Y., & Mizrahi, D. (1995). Configuring a seismographic
610 network for optimal monitoring of fault lines and multiple sources. *Bulletin of the seismological society of*
611 *America*, 85(6), 1847-1857.
- 612
- 613 Sokos, E., & Zahradník, J. (2013). Evaluating centroid-moment-tensor uncertainty in the new version of
614 ISOLA software. *Seismological Research Letters*, 84(4), 656-665.
- 615
- 616 Tape, W., & Tape, C. (2012). A geometric setting for moment tensors. *Geophysical Journal International*,
617 190(1), 476-498.
- 618
- 619 Tarantino, S., Colombelli, S., Emolo, A., & Zollo, A. (2019). Quick determination of the earthquake focal
620 mechanism from the azimuthal variation of the initial P-wave amplitude. *Seismological Research Letters*,
621 90(4), 1642-1649.
- 622
- 623 Trnkoczy, A., Bormann, P., Hanka, W., Holcomb, L. G., & Nigbor, R. L. (2009). Site selection, preparation
624 and installation of seismic stations. In *New Manual of Seismological Observatory Practice (NMSOP)* (pp. 1-
625 108). Deutsches GeoForschungsZentrum GFZ.
- 626
- 627 Vavrycuk, V., P. Adamova, J. Doubravová, and H. Jakoubková (2017). Moment Tensor Inversion Based on
628 the Principal Component Analysis of Waveforms: Method and Application to Microearthquakes in West
629 Bohemia, Czech Republic. *Seismological Research Letters* 88, 1303–1315, doi 10.1785/0220170027
- 630
- 631 Weber, E., Iannaccone, G., Zollo, A., Bobbio, A., Cantore, L., Corciulo, M., ... & Satriano, C. (2007).
632 Development and testing of an advanced monitoring infrastructure (ISNet) for seismic early-warning
633 applications in the Campania region of southern Italy. In *Earthquake early warning systems* (pp. 325-341).
634 Springer, Berlin, Heidelberg.
- 635
- 636 Zollo, A., & Bernard, P. (1991). Fault mechanisms from near-source data: joint inversion of S polarizations
637 and P polarities. *Geophysical Journal International*, 104(3), 441-451.
- 638

639
640
641
642
643
644
645
646
647
648
649
650
651
652

653
654
655
656
657
658
659
660
661
662
663
664
665
666
667
668
669
670
671
672
673
674
675
676
677
678
679
680
681
682
683
684
685
686

TABLES

Depth 5 km	Max Distance (km)	No. P-polarities
<i>M_L 1.0 -1.5</i>	30	1
<i>M_L 1.5 - 2.0</i>	49	1
<i>M_L 2.0 - 2.5</i>	57	4
Depth 10 km	Max Distance (km)	No. P-polarities
<i>M_L 1.0 -1.5</i>	33	1
<i>M_L 1.5 - 2.0</i>	40	5
<i>M_L 2.0 - 2.5</i>	66	6

Table 1 Maximum distance of the farthest triggered seismic station and number of P-wave polarities as function of earthquake magnitude and depth. The values, empirically derived from the ISNet bulletin, are used for the earthquake simulations.

687
688

Figure No.	Map	Focal Mechanism Solution	Magnitude Bin	Depth	Noise Level	Dataset
4	Kagan angle misfit	FM1, FM2, FM3	M3	10 km	5%	D1
5	Kagan angle misfit	FM1	M1, M2, M3	10 km	5%	D2, D3
6	focal mechanism parameter misfit	FM1	M1, M2, M3	10 km	5%	D3
7	Kagan angle average	FM1	M1, M2, M3	10 km	5%	D2, D3
8	Kagan angle standard deviation	FM1	M1, M2, M3	10 km	5%	D2, D3
9	focal mechanism error	FM1	M1, M2, M3	10 km	5%	D3
10	Kagan angle misfit	FM1, FM2, FM3	M1, M2, M3	10 km	5%	D3
11	focal mechanism parameter misfit	FM1	M1, M2, M3	5 km	5%	D3
12	Kagan angle misfit	FM1	M1, M2, M3	10 km	30%	D3

689
690
691
692
693
694
695
696
697
698
699
700
701
702
703
704
705
706
707
708
709
710
711
712

Table 2. Summary of the Figures 4-12 with parameters used for earthquake simulations whose results are represented as a specific map.

713
714

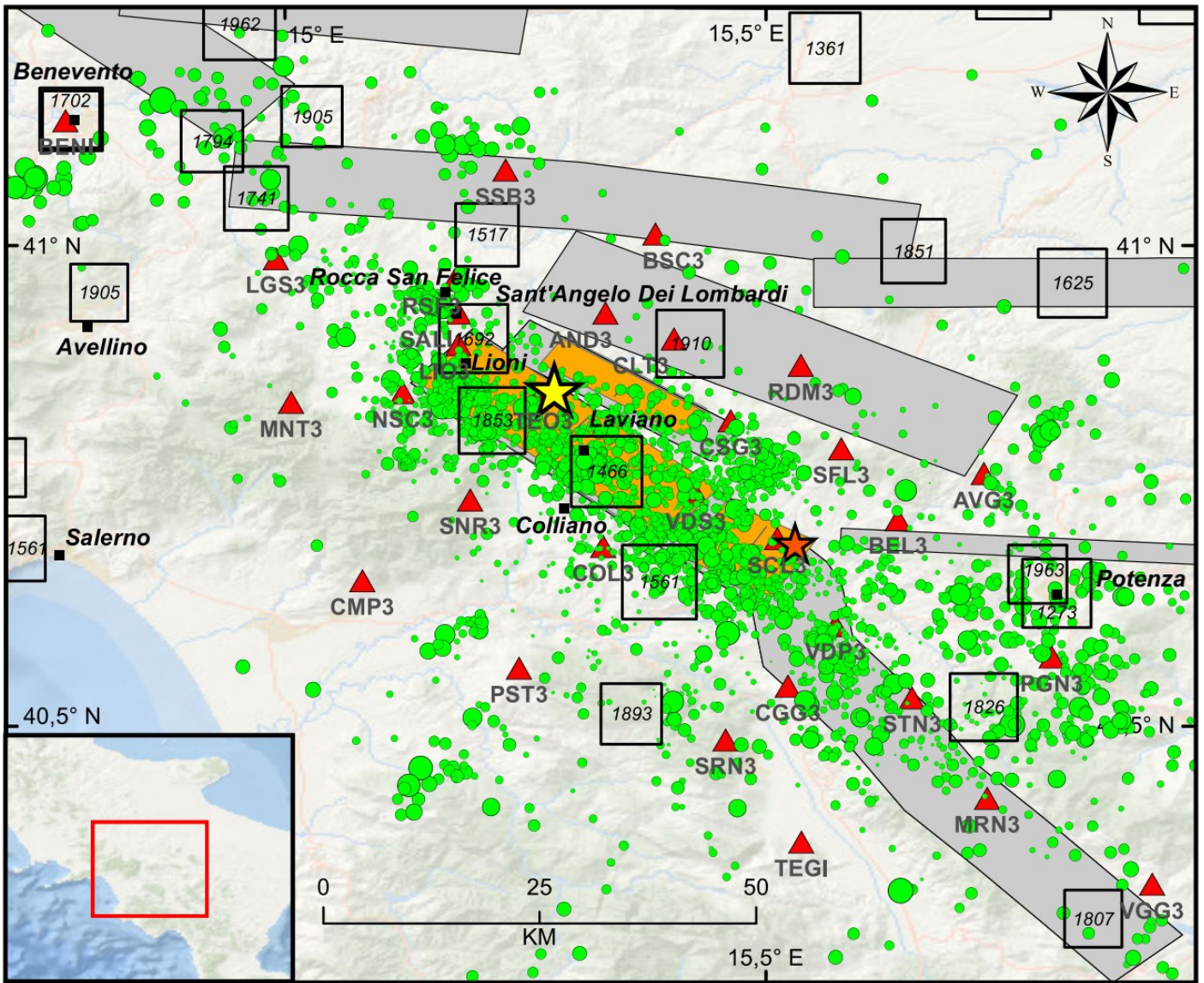
P-plunge (°)	P-trend (°)	T-plunge (°)	T-trend (°)	Strike (°)	Dip (°)	Rake (°)	Quality
55	344	31	196	325	20	-40	A
51	334	36	181	320	15	-30	A
55	14	31	226	355	20	-40	A
53	205	34	49	180	15	-40	A
55	72	33	272	35	15	-50	A
51	177	32	37	290	80	-110	A
54	292	34	91	10	80	-80	A
77	146	9	7	270	55	-100	B
80	235	10	55	325	55	-90	B
76	103	2	6	110	45	-70	B
76	117	2	214	290	45	-110	B
76	82	7	199	275	40	-110	B
75	190	15	10	280	60	-90	B
75	205	15	25	295	60	-90	B
85	230	5	50	140	40	-90	B
83	146	0	53	150	45	-80	B
80	240	10	60	330	55	-90	B
81	233	5	353	270	50	-80	B
81	347	5	227	130	50	-100	B
55	93	10	198	255	45	-140	C
55	133	10	238	295	45	-140	C
48	130	2	38	275	60	-140	C
48	305	2	37	340	60	-40	C
55	202	7	102	345	60	-130	C
58	121	2	27	270	55	-130	C
58	131	2	37	280	55	-130	C
55	342	7	242	125	60	-130	C
47	138	11	36	165	50	-30	C
49	182	14	289	340	45	-150	C
58	151	2	57	300	55	-130	C
49	168	14	61	190	45	-30	C
59	308	15	64	355	65	-60	C
57	306	14	59	115	40	-140	C
57	76	14	189	245	40	-140	C
45	85	6	348	225	65	-140	C
55	22	7	282	165	60	-130	C
57	241	14	354	50	40	-140	C
55	98	7	198	135	60	-50	C
51	115	2	22	145	55	-40	C
55	147	7	47	290	60	-130	C

715
716
717
718
719
720
721

Table 3. Fault plane solutions of instrumental seismicity occurred in Irpinia region in 2005-2008 and calculated by De Matteis et al., (2012). The solutions are classified according to a quality code based on the resolution of fault plane kinematics as derived in this study. The result of our simulations suggests a quality as follows: FM1=C, FM2=B, FM3=A.

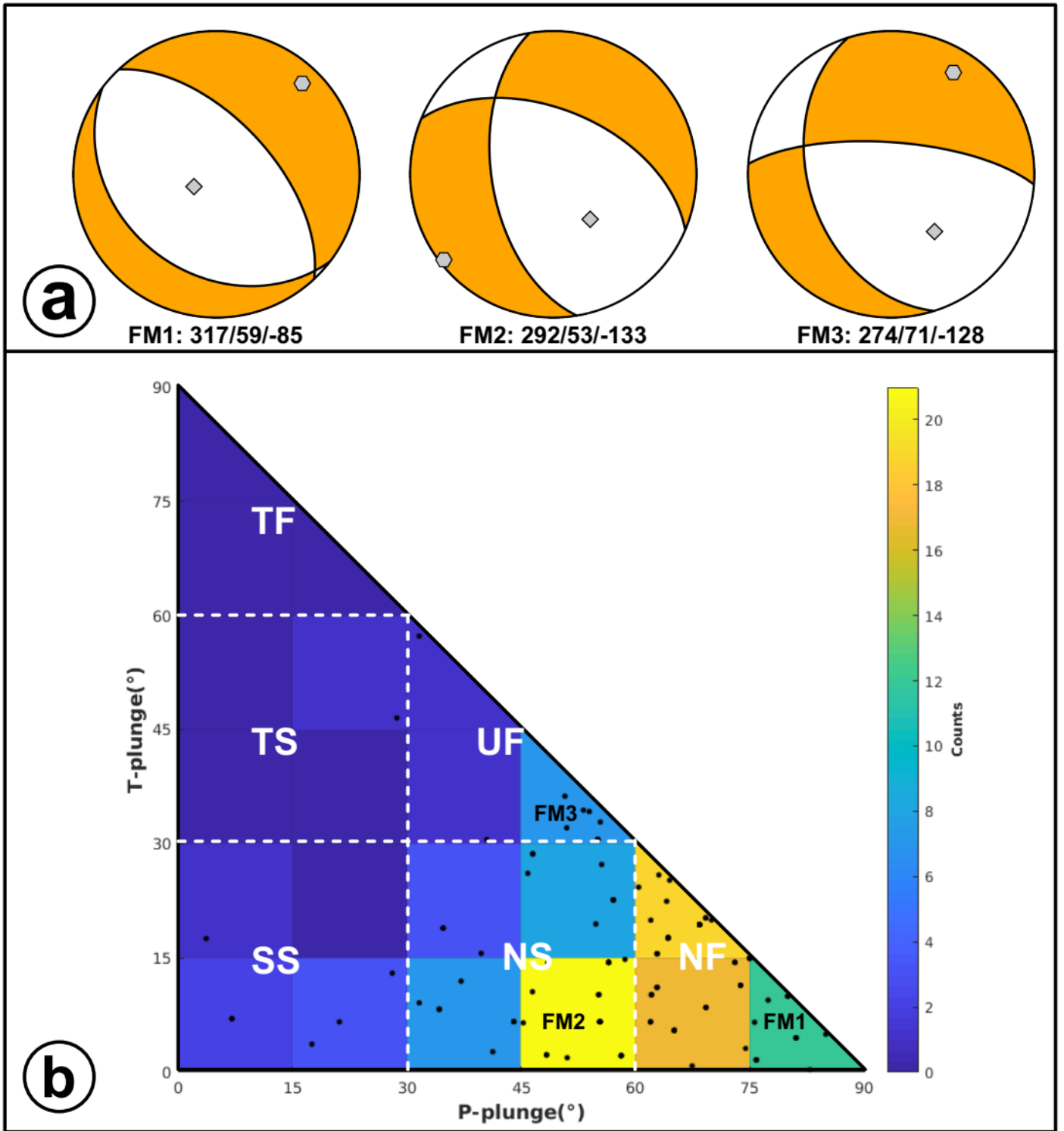
722
723
724
725
726

FIGURES



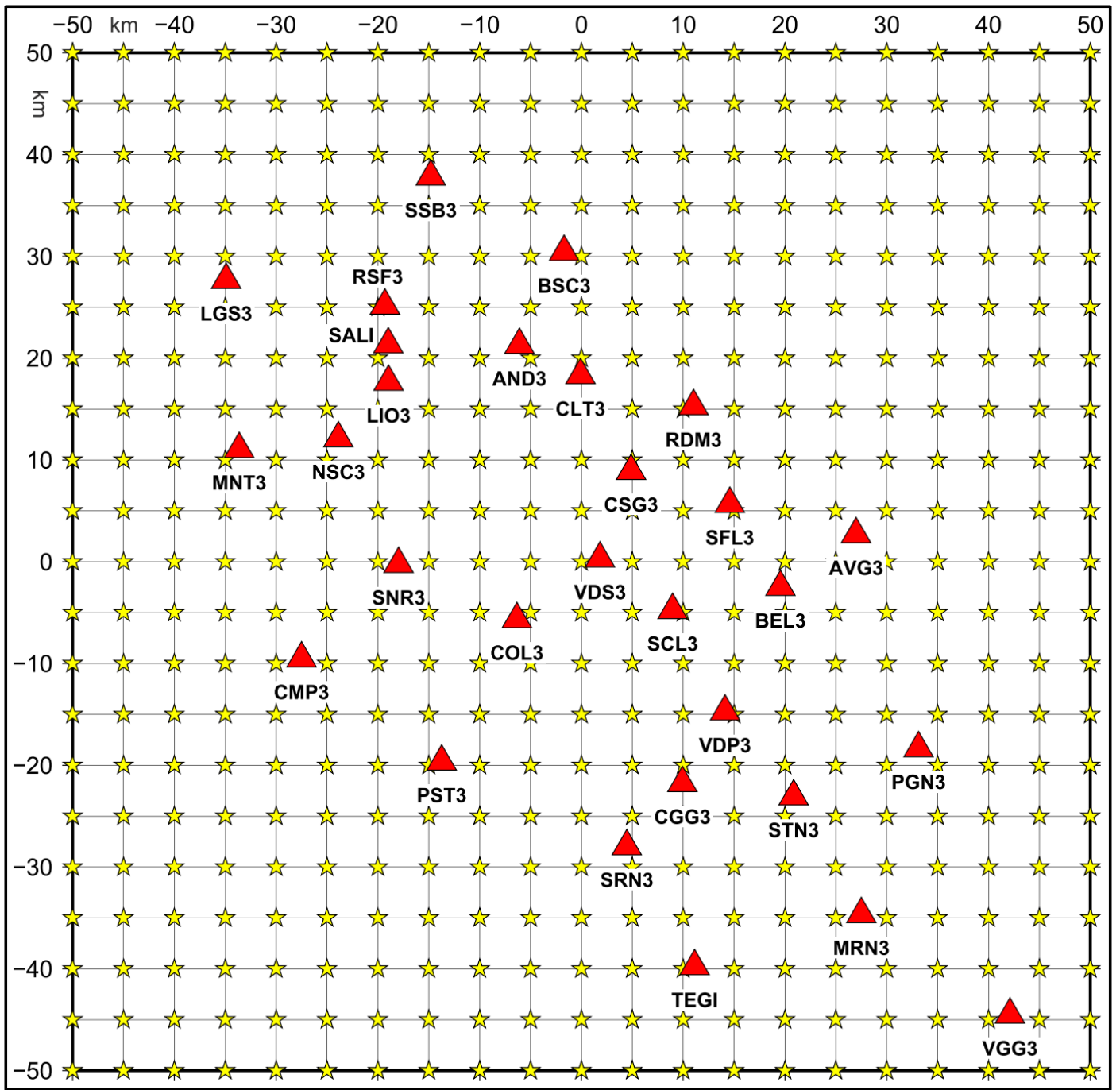
727
728
729
730
731
732
733
734
735
736
737
738
739
740

Figure 1. Epicentral map of the earthquakes (green circles) recorded by Irpinia Seismic Network (ISNet, red triangles) from 2008 to 2020 (<http://isnet-bulletin.fisica.unina.it/cgi-bin/isnet-events/isnet.cgi>). The yellow and orange stars refer to the epicentral location of the 1980, M 6.9, and of the 1996, M 4.9 earthquakes, respectively. Historical seismicity is shown with black squares ($IO \geq 6-7$ MCS). Seismogenic sources related to the Irpinia fault system are indicated by orange rectangles; potential sources for earthquakes larger than M 5.5 in surrounding areas are indicated in grey (Database of Individual Seismogenic Sources, DISS, Version 3.2.1)

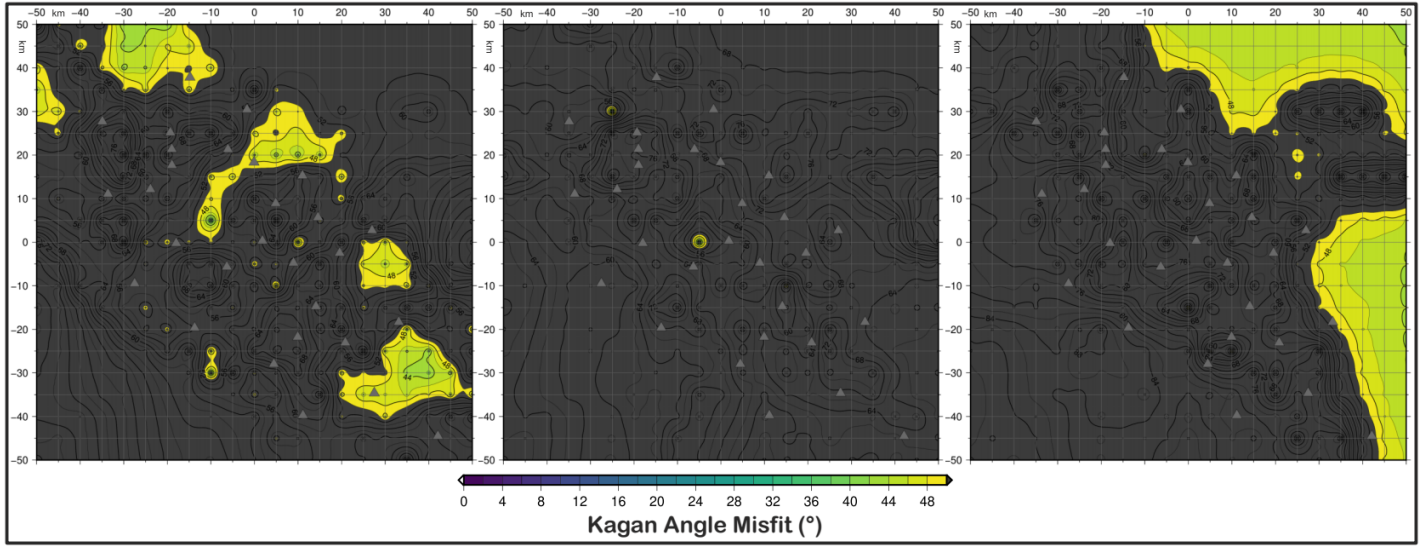


741
 742
 743
 744
 745
 746
 747
 748
 749
 750

Figure 2. Fault plane solutions used for earthquake simulations. a) From left to right: 1) Ms 6.9, 23rd November 1980 (FM1; Westaway) 2) and 3) Median focal mechanism found from solutions of the 1st (FM2) and 5th (FM3) most populated bin of histogram of panel b. b) Fault plane solutions (black dots) are classified according to the plunge of P- and T-axes with the specific tectonic regimes (Legend: NF, normal fault; NS, normal-strike; SS, strike-slip; TF, thrust ; TS, thrust-strike; UF, unknown fault). The number of earthquakes (colour bar) is counted in bins of 15° × 15°.

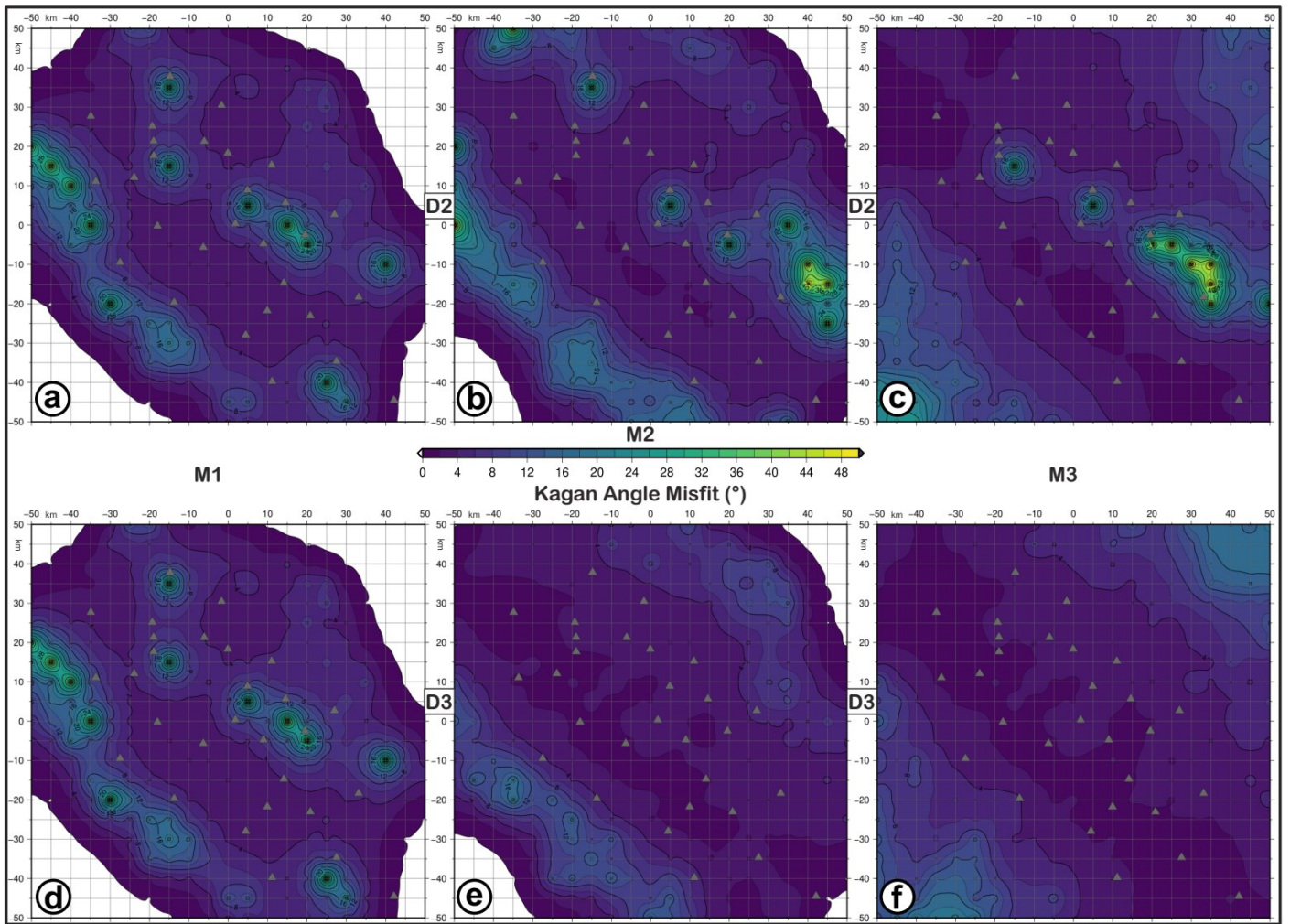


751
 752
 753 **Figure 3.** Regular grid of epicentres (yellow stars) used for simulating earthquakes. The area is 100x100
 754 km² with 5 km of spacing along both horizontal coordinates. Irpinia Seismic Network (ISNet) is reported
 755 with red triangles.
 756



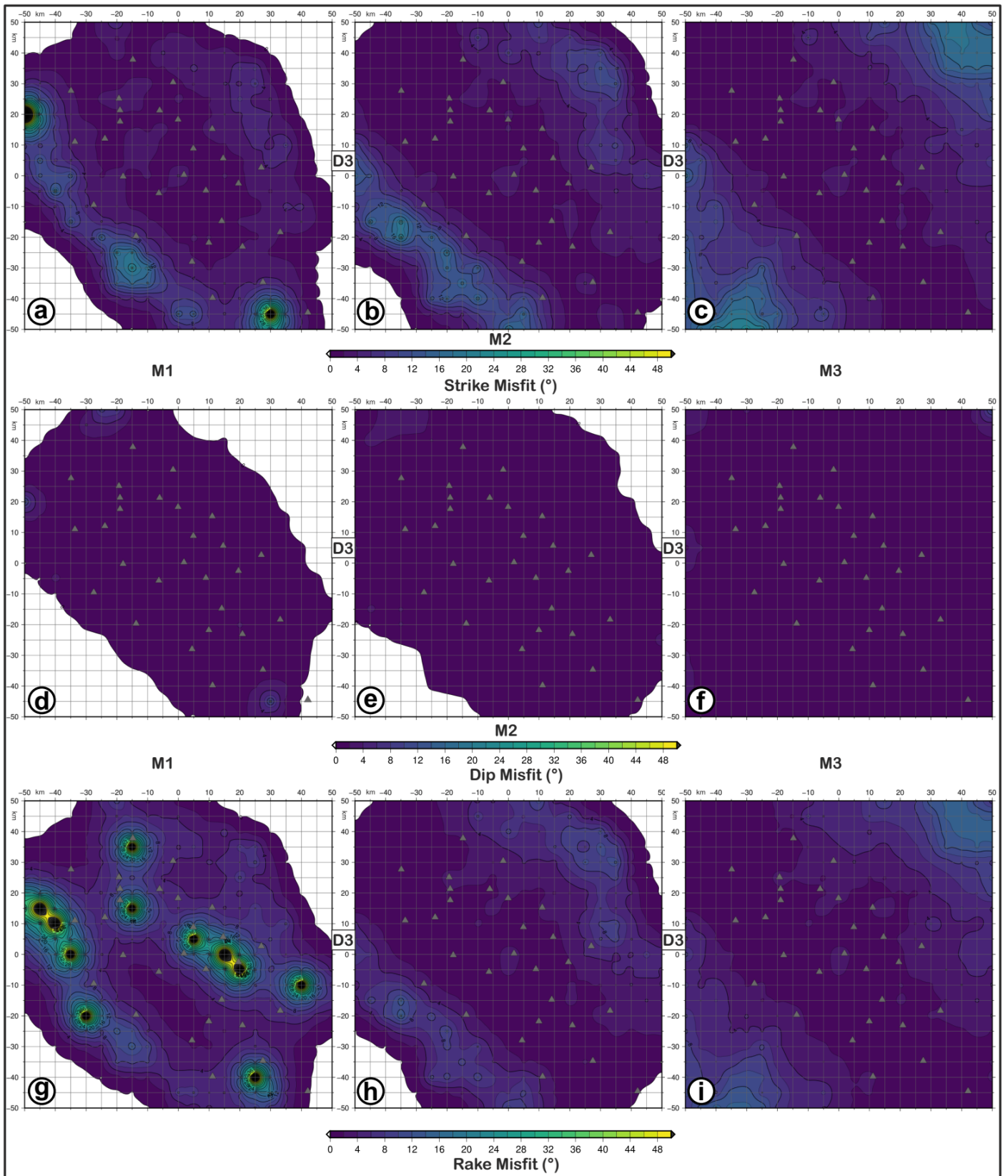
767
768
769
770
771
772
773
774
775
776
777
778
779
780
781
782
783
784
785
786
787
788
789
790
791
792
793
794
795
796

Figure 4. KAM (Kagan angle misfit) map for retrieved focal mechanisms with D1 dataset as input data and simulating earthquakes with M3 magnitude and FM1 (a), FM2 (b) and FM3 (c) theoretical fault plane solution at 10 km depth.

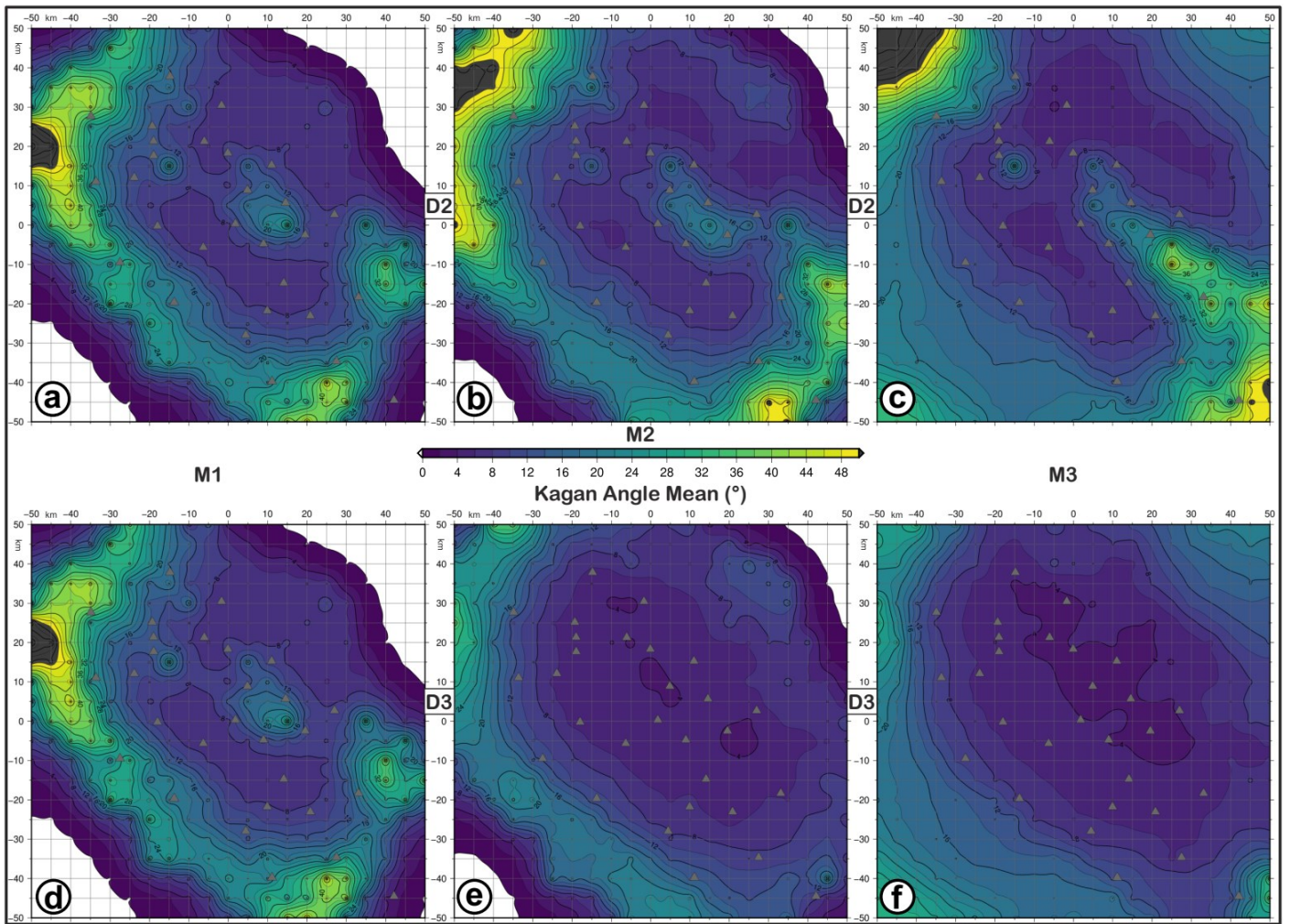


797
 798
 799 **Figure 5.** KAM (Kagan angle misfit) map for retrieved focal mechanisms with D2 (a, b, c) and D3 (d, e,
 800 f) datasets as input data and simulating earthquakes with M1 (a, d), M2 (b, e) and M3 (c, f) magnitudes
 801 and FM1 theoretical fault plane solution at 10 km depth. The level of Gaussian noise is set to 5%.

797
 798
 799
 800
 801
 802
 803
 804
 805

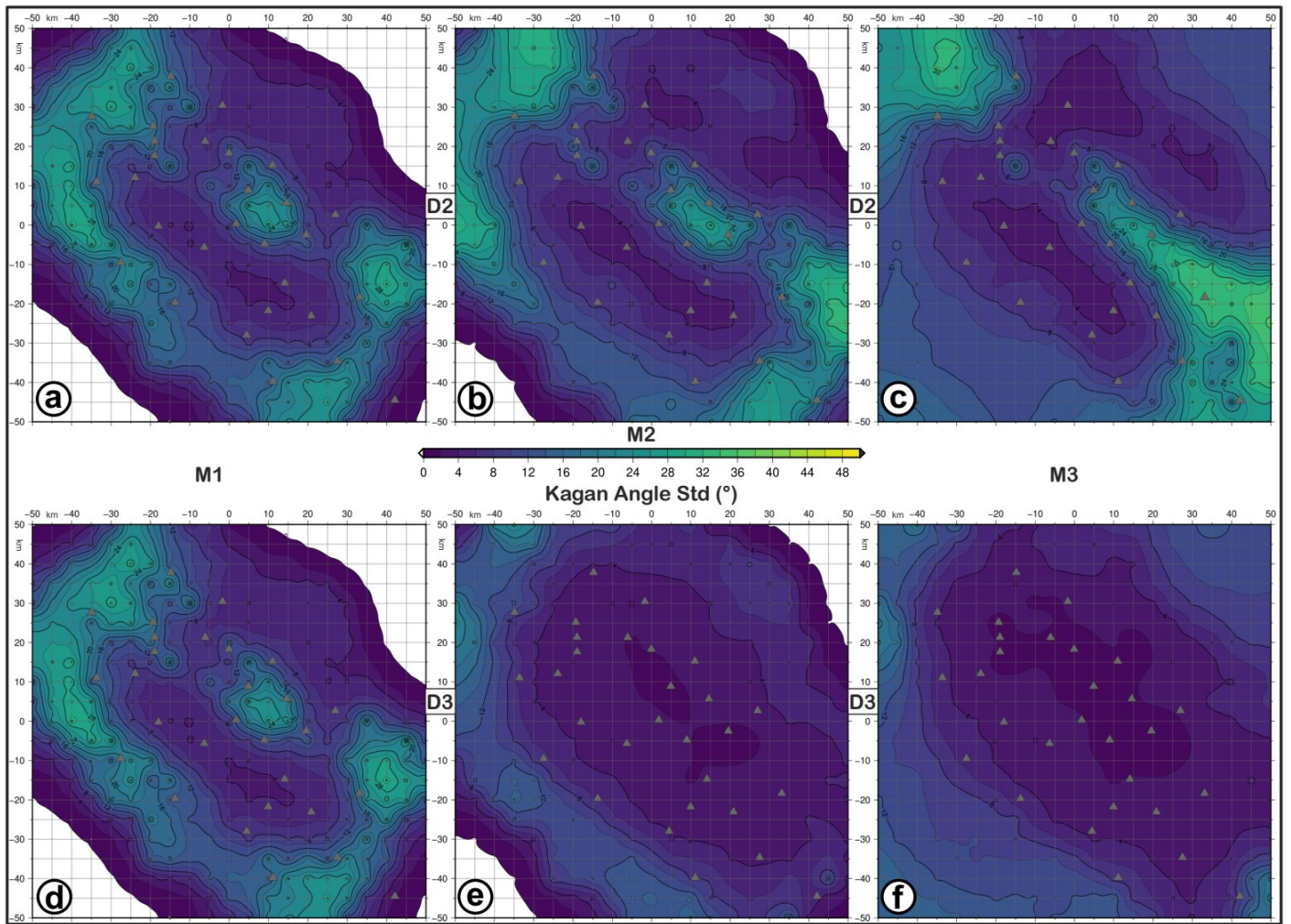


806
 807
 808 **Figure 6.** FMM (focal mechanism parameter misfit) maps for retrieved focal mechanisms with D3
 809 datasets as input data and simulating earthquakes with M1 (a, d, g), M2 (b, e, h) and M3 (c, f, i)
 810 magnitudes and FM1 theoretical fault plane solution at 10 km depth. a, b, c refer to strike misfit; d, e,
 811 f refer to dip misfit; g, h, i refer to rake. The level of Gaussian noise is set to 5%.
 812
 813



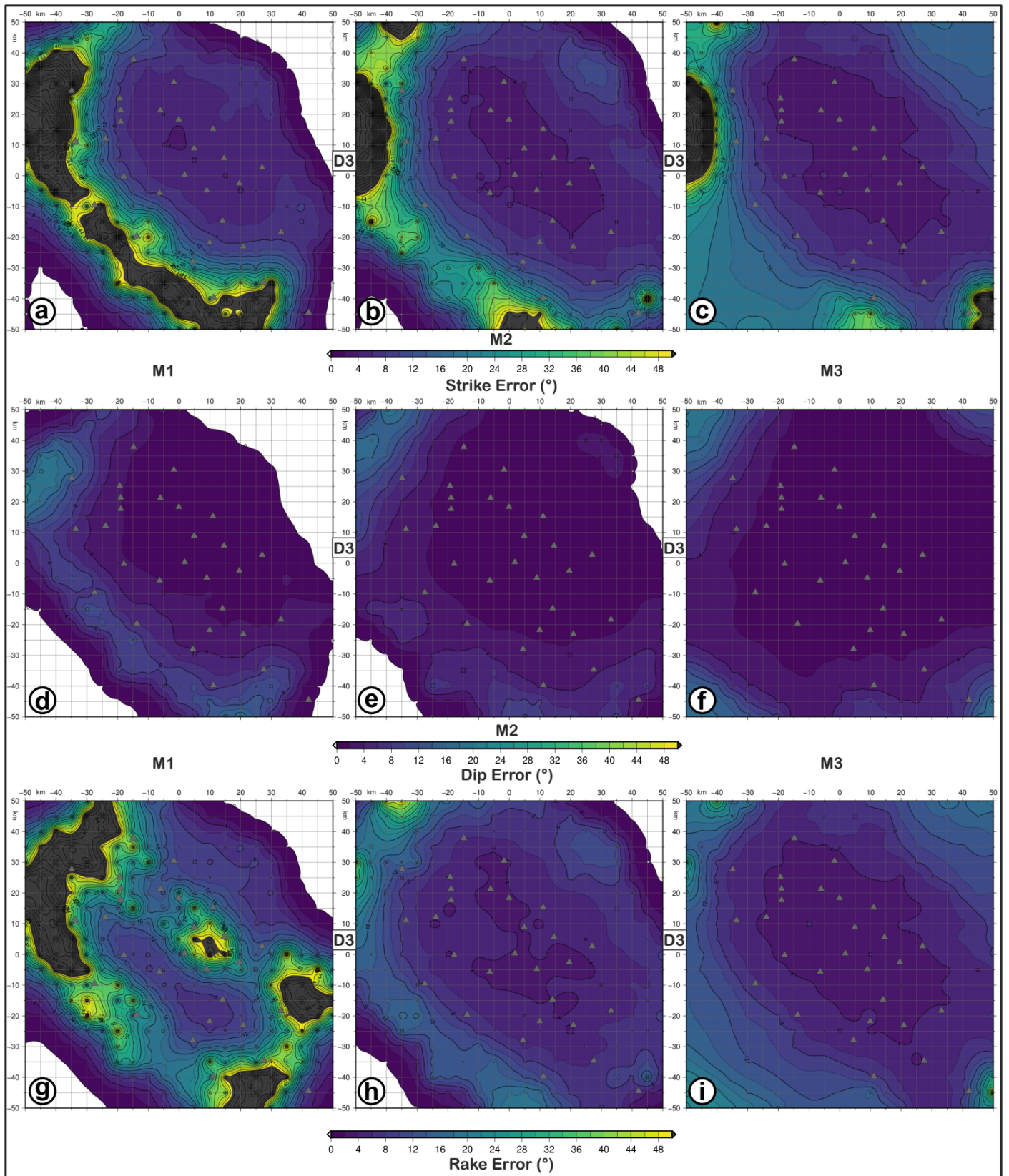
814
 815
 816 **Figure 7.** KAA (Kagan angle average) maps for retrieved focal mechanisms with D2 (a, b, c) and D3 (d, e, f) datasets as input data and simulating earthquakes with M1 (a, d), M2 (b, e) and M3 (c, f) magnitudes and FM1 theoretical fault plane solution at 10 km depth. The level of Gaussian noise is set to 5%.

814
 815
 816
 817
 818
 819
 820
 821
 822
 823
 824
 825
 826
 827
 828
 829
 830
 831



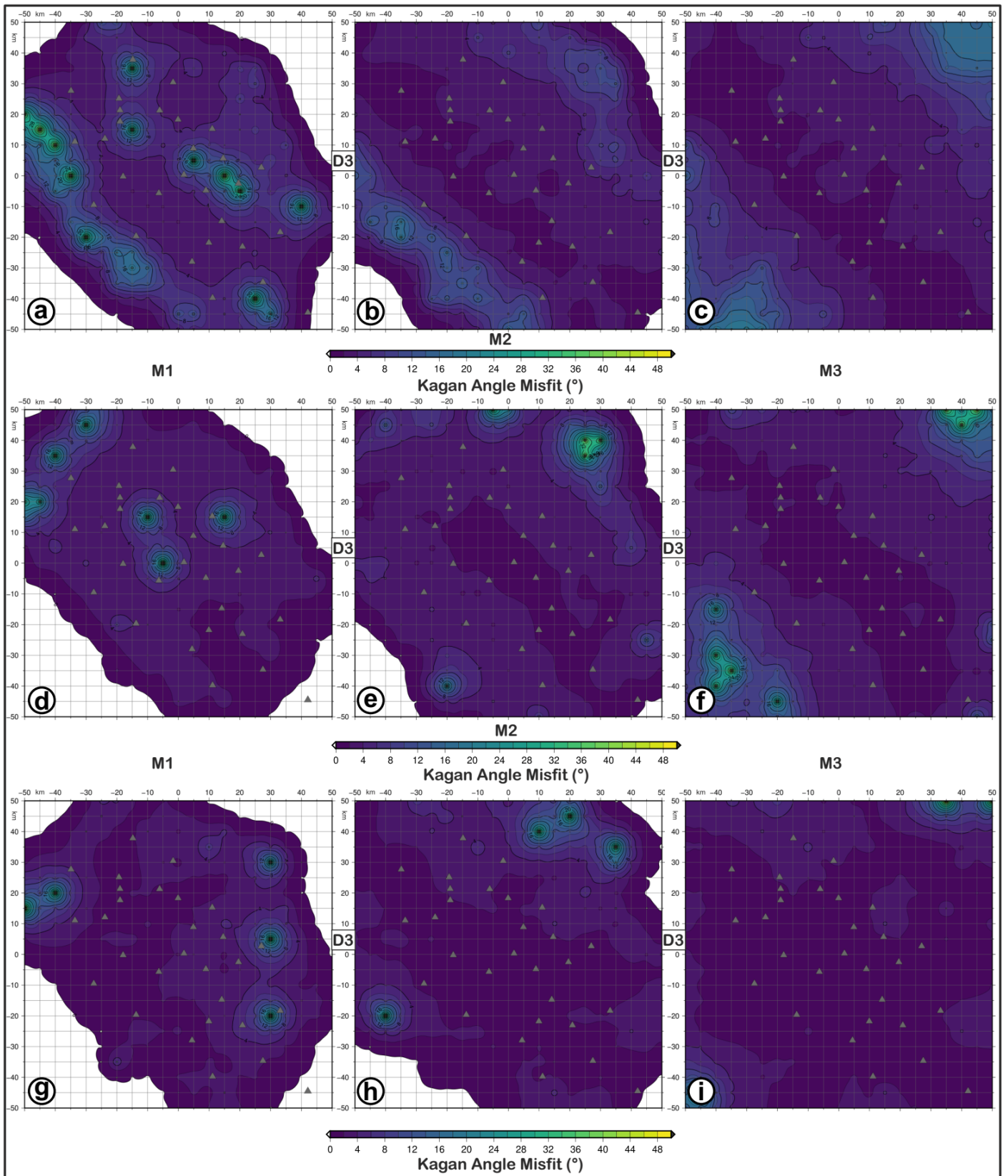
832
 833
 834 **Figure 8.** KAS (Kagan angle standard deviation) maps for retrieved focal mechanisms with D2 (a, b, c)
 835 and D3 (d, e, f) datasets as input data and simulating earthquakes with M1 (a, d), M2 (b, e) and M3 (c,
 836 f) magnitudes and FM1 theoretical fault plane solution at 10 km depth. The level of Gaussian noise is
 837 set to 5%.

832
 833
 834
 835
 836
 837
 838
 839
 840
 841
 842
 843
 844



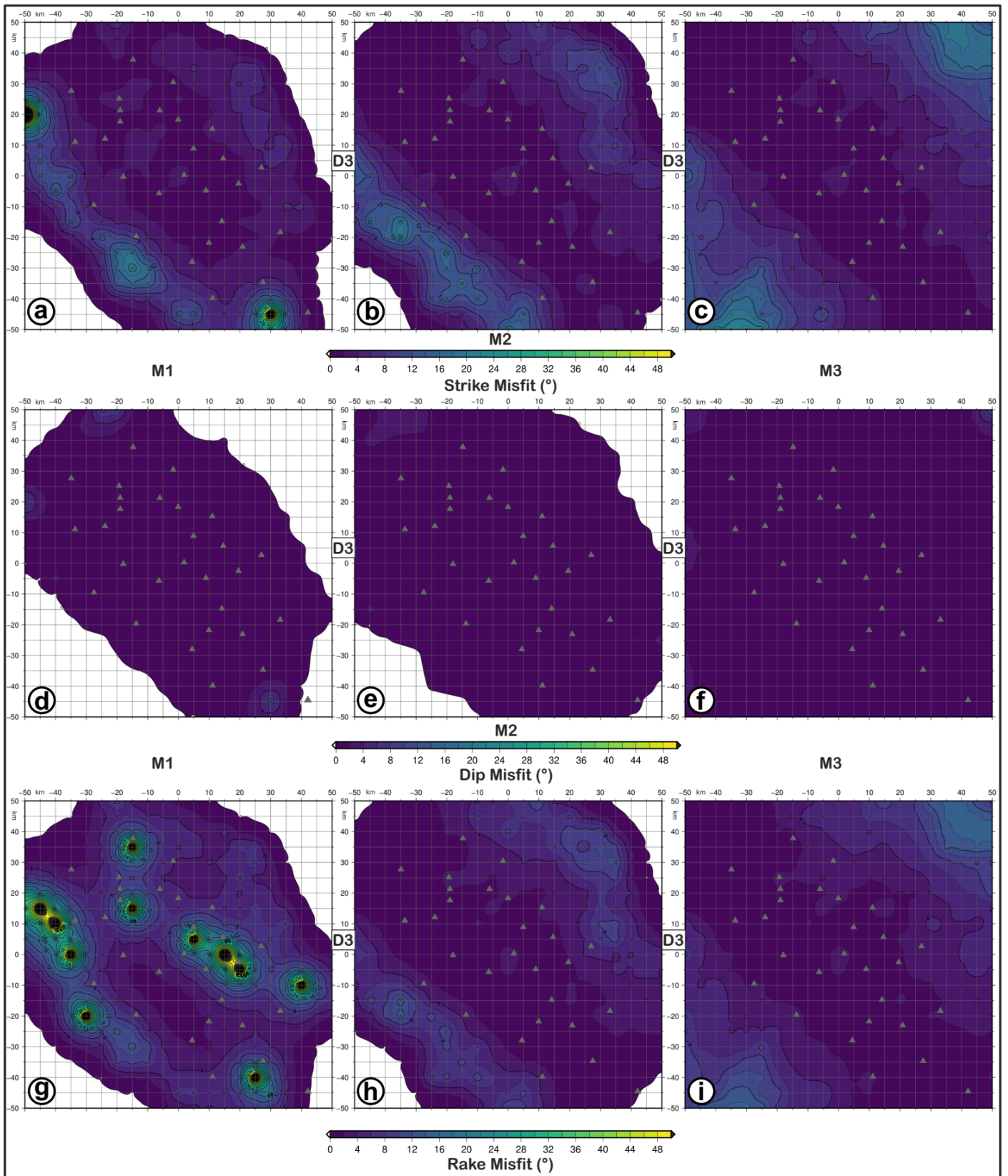
845
846
847
848
849
850
851
852

Figure 9. FME (strike, dip and rake error) maps for retrieved focal mechanisms with D3 datasets as input data and simulating earthquakes with M1 (a, d, g), M2 (b, e, h) and M3 (c, f, i) magnitudes and FM1 theoretical fault plane solution at 10 km depth. a, b, c refer to strike error; d, e, f refer to dip error; g, h, i refer to rake error. The level of Gaussian noise is set to 5%.



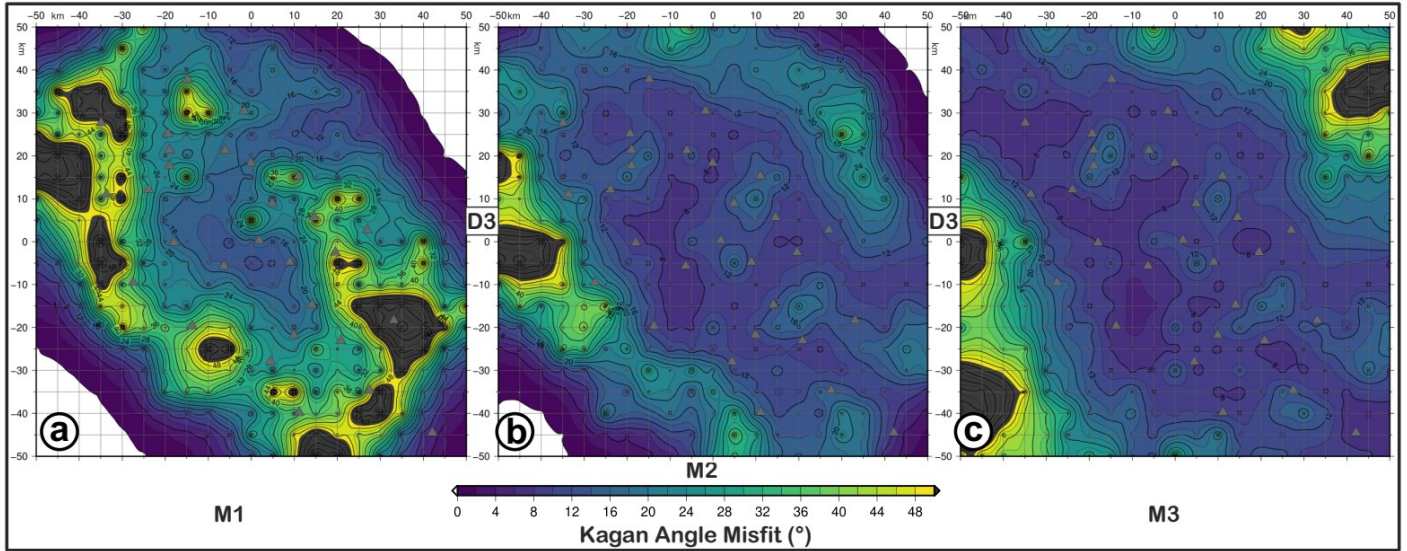
853
 854
 855
 856
 857
 858
 859
 860

Figure 10. KAM (Kagan angle misfit) maps for retrieved focal mechanisms with D3 datasets as input data and simulating earthquakes with M1 (a, d, g), M2 (b, e, h) and M3 (c, f, i) magnitudes and FM1 (a, b, c), FM2 (d, e, f) and FM3 (g, h, i) theoretical fault plane solution at 10 km depth. The level of Gaussian noise is set to 5%.



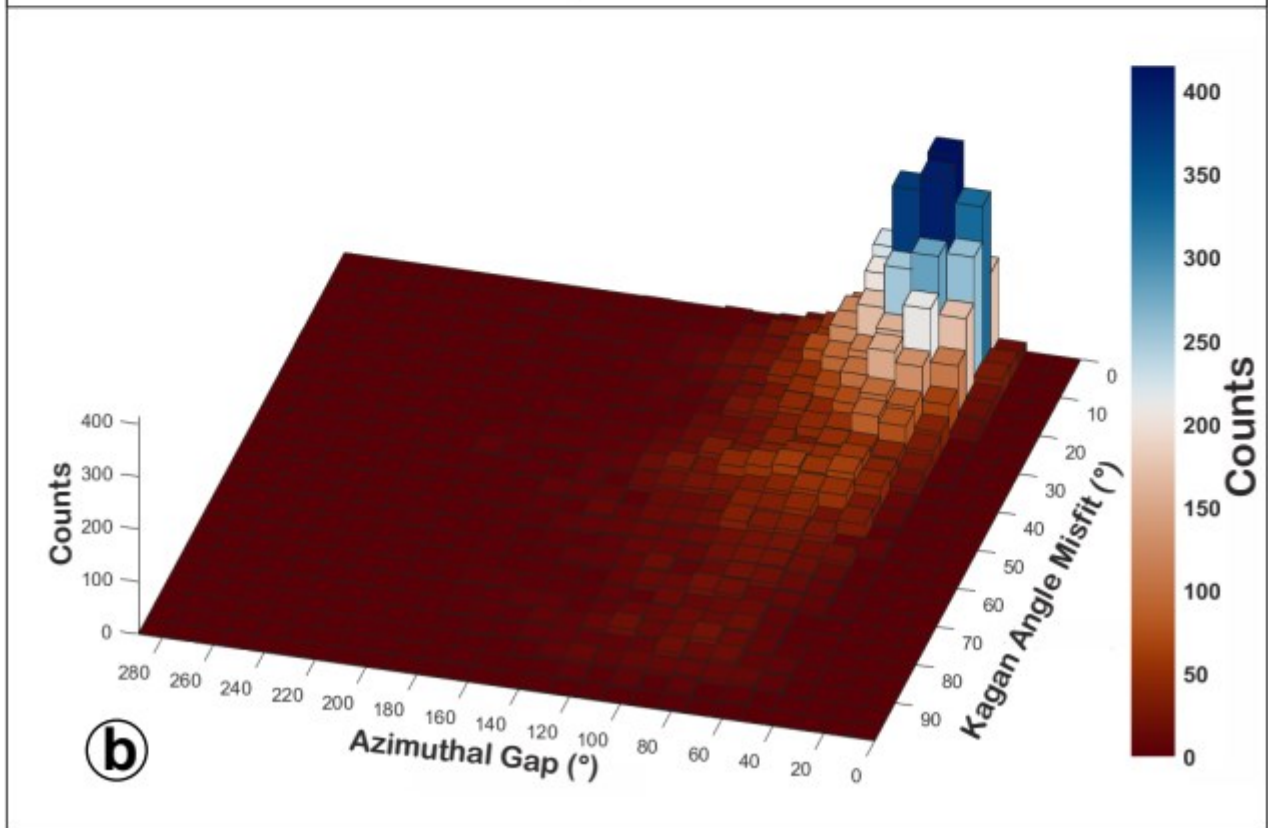
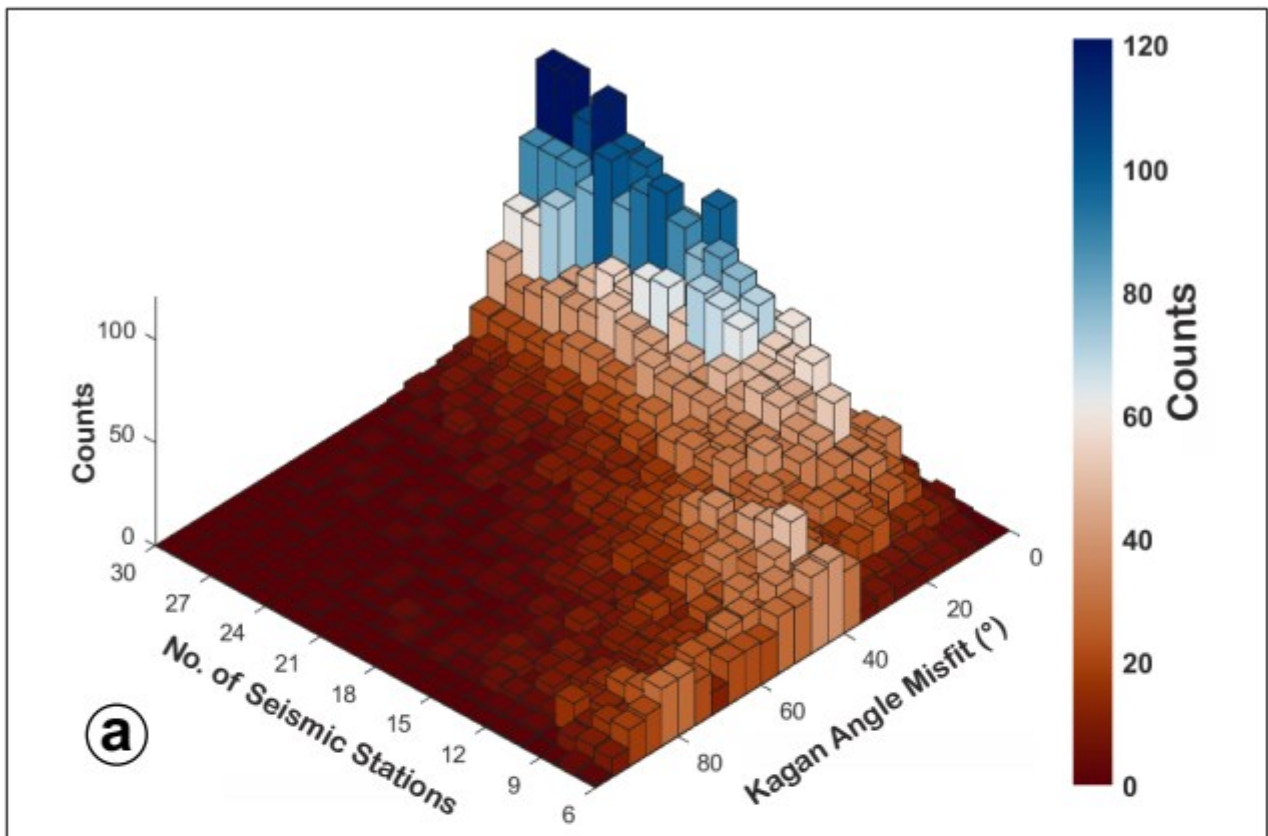
861
862
863
864
865
866
867
868

Figure 11. FMM (focal mechanism parameter misfit) maps for retrieved focal mechanisms with D3 datasets as input data and simulating earthquakes with M1 (a, d, g), M2 (b, e, h) and M3 (c, f, i) magnitudes and FM1 theoretical fault plane solution at 5 km depth. a, b, c refer to strike misfit; d, e, f refer to dip misfit; g, h, i refer to rake. The level of Gaussian noise is set to 5%.



870
871
872
873
874
875
876
877
878

Figure 12. KAM (Kagan angle misfit) map for retrieved focal mechanisms with D3 (a, b, c) datasets as input data and simulating earthquakes with M1 (a), M2 (b) and M3 (c) magnitudes and FM1 theoretical fault plane solution at 10 km depth. The level of Gaussian noise is set to 30%.



879
 880
 881
 882 **Figure 13.** 3D-histograms of the test results in terms of number of stations (a), azimuthal gap (b) and
 883 KA misfit. The simulations were carried out with a free network configuration.
 884
 885